IOP Publishing Smart Materials and Structures
Smart Mater. Struct. 25 (2016) 045022 (20pp) doi:10.1088/0964-1726/25/4/045022

A validated model for induction heating of shape memory alloy actuators

Robert N Saunders[1], James G Boyd[1], Darren J Hartl[1], Jonathan K Brown[2], Frederick T Calkins[2] and Dimitris C Lagoudas[1]

[1] Texas A and M University, Department of Aerospace Engineering, College Station, TX, USA
[2] Boeing Research and Technology, Seattle, WA, USA

E-mail: jgboyd@tamu.edu

Received 13 July 2015
Accepted for publication 11 December 2015
Published 14 March 2016

Abstract

Shape memory alloy (SMA) actuators deliver high forces while being compact and reliable, making them ideal for consideration in aerospace applications. One disadvantage of these thermally driven actuators is their slow cyclic time response compared to conventional actuators. Induction heating has recently been proposed to quickly heat SMA components. However efforts to date have been purely empirical. The present work approachs this problem in a computational manner by developing a finite element model of induction heating in which the time-harmonic electromagnetic equations are solved for the Joule heat power field, the energy equation is solved for the temperature field, and the linear momentum equations are solved to find the stress, displacement, and internal state variable fields. The combined model was implemented in Abaqus using a Python script approach and applied to SMA torque tube and beam actuators. The model has also been used to examine magnetic flux concentrators to improve the induction systems performance. Induction heating experiments were performed using the SMA torque tube, and the model agreed well with the experiments.

Keywords: induction heating, shape memory alloy, simulation, finite element analysis, electromagnetics, multiphysics

(Some figures may appear in colour only in the online journal)

1. Introduction

Shape memory alloys (SMAs) are active materials that provide lightweight, compact actuation with a high volume-specific mechanical energy density. SMAs can recover strains as large as 10% due to changes in temperature and/or stress [1]. The inelastic recoverable strain generated in the SMA is commonly referred to as transformation strain or actuation strain. This transformation strain is due to a diffusionless solid-to-solid transformation from a parent phase (austenite) to one or more crystallographic variants of martensite [2]. Although there is only a single variant of austenite, there can be many variants of martensite [3]. These martensite variants can be oriented under the appropriate application of stress and temperature, resulting in reconfigurable strains that can be recovered during martensitic transformation. This is known as the shape memory effect (SME) and provides a solid-state alternative in general actuation applications. Reliable SME must be 'trained' in the SMA by thermo–mechanically cycling the actuator under load in the direction of desired actuation until a stable hysteresis is achieved. Based on a number of factors, training may result in an SMA component that favors a particular internal distribution of oriented martensite variants that can generate and recover substantial deformations under no applied load. This behavior is known as the two-way SME. The most common form of SMA actuator is wire, which can actuate in a uniaxial tensile manner and, when they are formed into extensional springs, in a locally torsional manner. If actuation is desired in other directions, systems can be devised that allow these wires to be used, but such systems can become complex and inefficient in terms of volumetric energy density. To provide an alternative to wire-based solutions, recent developments have shown that SMA material can be processed and trained as large specimens with the ability to bend and twist under substantial loads [4].

Table 1. Potential heating and cooling methods for shape memory alloys.

Heating	Cooling
Direct resistive [25–28]	Free convection (air) [29]
Capacitance-assisted resistive [23]	Liquid immersion [30]
Conductive [16]	Forced air/liquid convection [29]
Convective [30]	Peltier effect [31]
Radiative (including laser) [32, 33]	Heat sinking [34]
Inductive [35]	*Cool Chips* technology[a] [21]

[a] Electron transport across a vacuum diode. Suitable for miniaturized applications such as micro-robotics.

SMA torsional actuators, commonly torque tubes, can be used for large-scale applications. SMA torque tubes are particularly useful for actuation in aerospace applications such as wing twisting [5–7], rotor blade twisting [8, 9], and space based radiator morphing [10, 11]. Since the primary mode of operation in SMA tubes is not tensile, the methods traditionally used to train and characterize SMA wires are not applicable. Many authors have developed reliable methods able to accurately characterize [12, 13] and model [14, 15] the behavior of torque tubes under a variety of thermal and mechanical loading conditions. In addition to torsional actuators, SMA bending beams have found application in the aerospace community. These beams have been characterized and modeled for a variety of aircraft [16, 17] and spacecraft [18, 19] applications as well as structural damping applications [20] beyond the aerospace industry.

While SMAs have a very high volumetric energy density compared to other actuators their actuation rate and frequency is limited by how quickly heat can be added and removed from the SMA component. Many authors suggest methods of heating and cooling [21–23], some of which are summarized in table 1. The size and shape of the SMA body greatly affects the choice of heating and cooling system implemented. Direct resistive heating is accepted as the most efficient heating method but such a method is generally current-limited to small and slender (i.e. wire) implementations. For large pieces, conductive and inductive heating become the best options. The speed of conductive heating is limited by distance (i.e. part size) and thermal conductivity, which is quite low in SMAs[3]. Inductive heating then becomes an attractive option to heat a large SMA component in a short time.

Induction heating is a non-contact heating method whereby an alternating current is input to a coil, inducing a time-harmonic electromagnetic field inside the coil. An electrically conductive workpiece in the vicinity of the coil and the field it generates experiences an induced internal current at the same frequency as the exciting frequency but having an opposite flow of current. Induction heating is commonly used in industrial manufacturing processes such as forging, material forming, heat treatment, or melting. The frequency utilized is relatively high ($\approx 10^4$–10^6 Hz(or $1/\mathrm{s}$)). Induction heating offers benefits over other heating methods, in particular conduction and convection, in terms of better thermal control and higher heating rate. The induced currents, known as *eddy currents*, result in a localized Joule heating effect in the workpiece. The induced currents are spatially non-uniform; their distribution depends on the workpiece shape, its electromagnetic properties, the eddy current frequency, the proximity of the workpiece to the coil, and the existence of other electrically conductive or magnetic bodies in the vicinity. The combination of these parameters affects the depth to which the magnetic field can penetrate the workpiece, known as the *skin effect*. A result of this skin effect is that 86% [36] of the heating power is often concentrated on the surface of a large conducting workpiece and the magnitude of the magnetic field decays exponentially as the distance from the surface increases. The penetration depth δ is defined as the distance from the workpiece surface at which the magnetic field has decayed to a factor of e^{-1} relative to its surface value [36] and is given by:

$$\delta = \sqrt{\frac{\rho}{\pi \mu_0 \mu_\mathrm{r} f}}, \tag{1}$$

where ρ is the electrical resistivity, μ_0 is the magnetic permeability of vacuum ($4\pi \times 10^{-7}\ \mathrm{H\,m^{-1}}$), μ_r is the relative magnetic permeability, and f is the frequency in Hz of the current.

Induction heating has recently been applied to a number of active material applications in an experimental manner. For example, work with shape memory polymers has shown that magnetic nanoparticles embedded in the polymer matrix allow the material to achieve faster heating and in turn faster actuation [37, 38]. In alloy manufacturing, induction heating is used as a method to quickly and cheaply melt pure metals (i.e. Ni-pellets and Ti-rods); in SMA production, this yields a material that has a better chemical homogeneity relative to other methods [39–41]. Induction heating had been implemented in SMA medical device applications as it offers a method of non-contact heating whereby only the SMA component is heated while the surrounding material is not [42–45]. Outside of the medical device industry, Hamilton *et al* used induction heating to heat grips for testing a single crystal SMA specimen [46], Wetzel used induction heating to actuate an SMA piece in a controlled de-bonding application [47], and Webster considered the use of induction heating for SMA components associated with an adaptable turbine exhaust [35, 48]. To fully understand how active materials and induction heating interact, predictive analytical/computational studies of SMA components in an electromagnetic field is desired. Takagi *et al* [49] showed simulations of an electromagnetic field in an SMA plate using a phenomenological model, but that work does not develop such a model for a general component. There are also reduced-order models for both the pseudoelastic torsional behavior of SMA tubes [15] and induction heating of tubes [36], which can be combined to address the problem but again these models would not account for induction heating heating of general SMA actuators.

[3] Approximately 5% that of a pure aluminum [24].

The goal of the research reported herein was to develop and demonstrate for the first time a 3D spatial and temporal finite element model for induction heating of SMA actuators toward future design and optimization efforts. The paper is organized as follows: the governing equations are presented in section 2. The procedure for determining the electromagnetic and thermo–mechanical material constants for an SMA torsional tube is presented in section 3. An SMA torque tube and an SMA beam actuator are simulated in section 4. Conclusions and future work are presented in section 5.

2. Governing equations

The objective in analyzing an SMA actuator is to understand the spatial and temporal distributions of stresses, strains, internal state variables (i.e. transformation variables), and temperature throughout the body. The necessary equations are presented in this section. In this work we assume small deformations so that the material time derivative $\mathrm{d}/\mathrm{d}t$ can be replaced by the local time derivative $\partial/\partial t$, which is denoted by an overhead dot i.e. $(\dot{\cdot})$. We also denote the magnitude of a vector as $|\cdot|$ and the magnitude of a complex vector is given by $(\cdot)(\cdot)^*$, where the * is the complex conjugate of the vector.

2.1. Physical principles

In general the conservation of linear momentum [50] requires universal local satisfaction of

$$\nabla \cdot \boldsymbol{\sigma} + \boldsymbol{f} = 0, \tag{2}$$

where $\boldsymbol{\sigma}$ is the (symmetric) Cauchy stress tensor. However in this work, the electromagnetic and gravitation body forces [51]

$$\boldsymbol{f} = \rho^{\mathrm{c}}\boldsymbol{E} + (\nabla \boldsymbol{E})\boldsymbol{P} + \boldsymbol{J} \times \boldsymbol{B} + (\boldsymbol{B}\nabla)^{\mathrm{T}}\boldsymbol{M} + \rho^{\mathrm{m}} g \tag{3}$$

are assumed to be negligible. In these equations, ρ^{c} is the free electric charge density, $\boldsymbol{E}$ is the electric field intensity, $\boldsymbol{P}$ is the polarization, $\boldsymbol{J}$ is the current density, $\boldsymbol{B}$ is the magnetic flux density, $\boldsymbol{M}$ is the magnetization, ρ^{m} is the mass density, and g is the gravitational constant. The linear strain-displacement equations [50] are used:

$$\varepsilon = \frac{1}{2}[\nabla \boldsymbol{u} + (\nabla \boldsymbol{u})^{\mathrm{T}}], \tag{4}$$

where ε is the total strain tensor and $\boldsymbol{u}$ is the displacement vector. The first law of thermodynamics is written as

$$\rho^{\mathrm{m}}\dot{u} = \boldsymbol{\sigma} : \dot{\varepsilon} + \boldsymbol{E} \cdot \dot{\boldsymbol{D}} + \boldsymbol{H} \cdot \dot{\boldsymbol{B}} + \boldsymbol{E} \cdot \boldsymbol{J} - \nabla \cdot \boldsymbol{q}, \tag{5}$$

where u is the specific internal energy, $\boldsymbol{H}$ is the magnetic field intensity, $\boldsymbol{D}$ is the electric displacement, and $\boldsymbol{q}$ is the conduction heat flux vector. In addition to the first law, the second law must be used to develop thermodynamically consistent constitutive equations. The second law can be written in the form of the Clausius–Planck inequality [1] as

$$\rho^{\mathrm{m}}\dot{s} + \nabla \cdot \boldsymbol{q} \geqslant 0, \tag{6}$$

where s is the entropy. Time varying electromagnetic fields such as those in induction heating are described by Maxwell's equations in the local form using a magneto-quasi-static approximation (frequencies below about 10^9 Hz the rate of charge displacement, $\dot{\boldsymbol{D}}$, is negligible compared to the conduction current.) [52–54] as

$$\nabla \times \boldsymbol{H} = \boldsymbol{J} \quad \text{(Ampere's law)}, \tag{7a}$$

$$\nabla \times \boldsymbol{E} = -\dot{\boldsymbol{B}} \quad \text{(Faraday's law)}, \tag{7b}$$

$$\nabla \cdot \boldsymbol{B} = 0 \quad \text{(Gauss' law for magnetism)}. \tag{7c}$$

2.2. Constitutive equations

In this work all material properties are assumed to be isotropic. A Gibbs free energy is chosen with the following independent variables, $G = G(\boldsymbol{\sigma}, T, \boldsymbol{D}, \boldsymbol{B}, \varepsilon^{\mathrm{t}}, \xi, g^{\mathrm{t}})$, where T is the temperature, ε^{t} is the transformation strain tensor, ξ denotes the martensite volume fraction, and g^{t} is the transformation hardening energy. The Coleman–Noll procedure [55, 56] can be applied to derive

$$s = -\frac{\partial G}{\partial T}, \tag{8a}$$

$$\varepsilon = -\rho^{\mathrm{m}}\frac{\partial G}{\partial \boldsymbol{\sigma}}, \tag{8b}$$

$$\boldsymbol{E} = \rho^{\mathrm{m}}\frac{\partial G}{\partial \boldsymbol{D}}, \tag{8c}$$

$$\boldsymbol{H} = \rho^{\mathrm{m}}\frac{\partial G}{\partial \boldsymbol{B}}. \tag{8d}$$

Application of the second law of thermodynamics results in a dissipation inequality, which we assume can be decomposed into the following three inequalities

$$\boldsymbol{E} \cdot \boldsymbol{J} \geqslant 0, \tag{9a}$$

$$-\boldsymbol{q} \cdot \nabla T \geqslant 0, \tag{9b}$$

$$\frac{\partial G}{\partial \varepsilon^{\mathrm{t}}} : \dot{\varepsilon}^{\mathrm{t}} + \frac{\partial G}{\partial \xi}\dot{\xi} + \frac{\partial G}{\partial g^{\mathrm{t}}}\dot{g}^{\mathrm{t}} \geqslant 0. \tag{9c}$$

The first two inequalities are able to be decoupled by neglecting thermal electric effects (Seebeck and Peltier) and the third represents the generalized thermodynamical forces [1, 57]. The form of the free energy is chosen so that the magnetic constitutive relations, Ohm's law, and Fourier's law are given by

$$\boldsymbol{B} = \mu_0 \mu_{\mathrm{r}} \boldsymbol{H}, \tag{10a}$$

$$\boldsymbol{E} = \rho \boldsymbol{J}, \tag{10b}$$

$$\boldsymbol{q} = -k\nabla T. \tag{10c}$$

where μ_0 is the magnetic permeability of free space, μ_{r} is the relative magnetic permeability, ρ is the electrical resistivity, and k is the thermal conductivity.

There are many models that describe SMA behavior [58, 59]. The model chosen herein was developed by Lagoudas *et al* [1, 3, 57]. This model is computationally efficient and has been proven experimentally accurate under a variety of thermo–mechanical loading conditions [60]. The model has recently been modified by Hartl *et al* to account for

the effects of plasticity [61] and transformation induced anisotropy [62, 63].

Because the electromagnetic and thermomechanical terms in the free energy are assumed to be uncoupled, the thermomechanical specific Gibbs free energy due to the austenite, martensite, and mixed phases is given by the rule of mixtures as

$$G^{\mathrm{SMA}}(\boldsymbol{\sigma}, T, \varepsilon^{\mathrm{t}}, \xi, g^{\mathrm{t}}) = G^{\mathrm{A}}(\boldsymbol{\sigma}, T) + \xi[G^{\mathrm{M}}(\boldsymbol{\sigma}, T) - G^{\mathrm{A}}(\boldsymbol{\sigma}, T)] + G^{\mathrm{mix}}(\boldsymbol{\sigma}, \varepsilon^{\mathrm{t}}, g^{\mathrm{t}}). \tag{11}$$

G^{A} and G^{M} represent the Gibbs free energy in the austenite and martensite phases respectively. Assuming a quadratic stress dependence, G^{ζ} for $\zeta = A, M$ gives

$$G^{\zeta}(\boldsymbol{\sigma}, T) = -\frac{1}{2\rho^{\mathrm{m}}}\boldsymbol{\sigma} : \boldsymbol{S}^{\zeta}\boldsymbol{\sigma} - \frac{1}{\rho^{\mathrm{m}}}\boldsymbol{\sigma} : \boldsymbol{\alpha}^{\zeta}(T - T_0) + c^{\zeta}\left[(T - T_0) - T\ln\left(\frac{T}{T_0}\right)\right] - s_0^{\zeta}T + u_0^{\zeta} \tag{12}$$

and the mixing term is given as

$$G^{\mathrm{mix}}(\boldsymbol{\sigma}, \varepsilon^{\mathrm{t}}, g^{\mathrm{t}}) = -\frac{1}{\rho^{\mathrm{m}}}\boldsymbol{\sigma} : \varepsilon^{\mathrm{t}} + \frac{1}{\rho^{\mathrm{m}}}g^{\mathrm{t}}. \tag{13}$$

The parameters $\boldsymbol{S}$, T_0, s_0, and u_0 are the compliance tensor, reference temperature, specific reference entropy, and specific reference internal energy. The values of $\boldsymbol{S}$, s_0, and u_0 are all assumed to be dependent on the phase of the material. The specific heat c, density ρ^{m}, and the second-order coefficient of thermal expansion $\boldsymbol{\alpha}$ are assumed constant regardless of phase. The phase-dependent parameters are also evaluated by a rule of mixtures in terms of ξ. For example, the compliance tensor $\boldsymbol{S}(\xi)$ is found as

$$\boldsymbol{S}(\xi) = \boldsymbol{S}^{\mathrm{A}} + \xi(\boldsymbol{S}^{\mathrm{m}} - \boldsymbol{S}^{\mathrm{A}}) = \boldsymbol{S}^{\mathrm{A}} + \xi\tilde{\boldsymbol{S}}. \tag{14}$$

Now using the procedure of Coleman–Noll, the total strain and entropy are obtained as

$$\varepsilon = -\rho^{\mathrm{m}}\frac{\partial G}{\partial \boldsymbol{\sigma}} = \boldsymbol{S}(\xi)\boldsymbol{\sigma} + \boldsymbol{\alpha}(\xi)(T - T_0) + \varepsilon^{\mathrm{t}} \tag{15}$$

and

$$s = -\frac{\partial G}{\partial T} = \frac{1}{\rho^{\mathrm{m}}}\boldsymbol{\sigma} : \boldsymbol{\alpha} + c\ln\left(\frac{T}{T_0}\right) + s_0. \tag{16}$$

Equation (15) can be rewritten in a more common form as Hooke's law,

$$\boldsymbol{\sigma} = \boldsymbol{S}^{-1}\,\varepsilon^{\mathrm{el}} = \boldsymbol{S}^{-1}[\varepsilon - \varepsilon^{\mathrm{t}} - \boldsymbol{\alpha}(T - T_0)]. \tag{17}$$

The evolution equations governing the transformation strain and hardening are given as

$$\dot{\varepsilon}^{\mathrm{t}} = \dot{\xi}\boldsymbol{\Lambda}^{\mathrm{t}}, \tag{18a}$$

$$\dot{g}^{\mathrm{t}} = f^{\mathrm{t}}\dot{\xi}, \tag{18b}$$

$$\boldsymbol{\Lambda}^{\mathrm{t}}(\overline{\sigma}^{\mathrm{eff}}) = \begin{cases} \frac{3}{2}H^{\mathrm{cur}}(\overline{\sigma}^{\mathrm{eff}})\frac{\boldsymbol{s}^{\mathrm{eff}}}{\overline{\sigma}^{\mathrm{eff}}}; & \dot{\xi} > 0, \\ \frac{\varepsilon^{\mathrm{t-r}}}{\xi^{\mathrm{r}}}; & \dot{\xi} < 0, \end{cases} \tag{18c}$$

$$H^{\mathrm{cur}}(\overline{\sigma}^{\mathrm{eff}}) = H_{\max}(1 - \mathrm{e}^{k^{\mathrm{t}}\overline{\sigma}^{\mathrm{eff}}}), \tag{18d}$$

$$\boldsymbol{\sigma}^{\mathrm{eff}} = (\boldsymbol{\sigma} + \boldsymbol{\beta}), \tag{18e}$$

where $H_{\max}$ is the maximum uniaxial transformation strain, $\boldsymbol{s}^{\mathrm{eff}}$ is the deviatoric effective stress, $\varepsilon^{\mathrm{t-r}}$ is the transformation strain tensor at cycle reversal, ξ^{r} is the martensitic volume fraction at reversal, $\boldsymbol{\beta}$ is the back stress tensor developed during previous processing and training and which does not evolve in this case, k^{t} is a parameter that controls the rate at which H^{cur} evolves exponentially, $\overline{\sigma}^{\mathrm{eff}}$ is the Mises equivalent of the effective stress given as

$$\overline{\sigma}^{\mathrm{eff}} = \sqrt{\frac{3}{2}\boldsymbol{s}^{\mathrm{eff}} : \boldsymbol{s}^{\mathrm{eff}}} \tag{19}$$

and f^{t} is given for forward and reverse transformation as

$$f^{\mathrm{t}} = \begin{cases} \frac{1}{2}a_1(1 + \xi^{n_1} - (1 - \xi)^{n_3}) + a_3; & \dot{\xi} > 0, \\ \frac{1}{2}a_2(1 + \xi^{n_3} - (1 - \xi)^{n_4}) - a_3; & \dot{\xi} < 0. \end{cases} \tag{20}$$

A transformation function constraining the evolution of the martensitic volume fraction is postulated such that

$$\Phi^{\mathrm{t}} = \begin{cases} \Phi^{\mathrm{t}}_{\mathrm{fwd}} = \Pi - Y^{\mathrm{t}}; & \dot{\xi} > 0, \\ \Phi^{\mathrm{t}}_{\mathrm{rev}} = -\Pi - Y^{\mathrm{t}}; & \dot{\xi} < 0 \end{cases} \tag{21}$$

which is constrained in the manner of classical plasticity so that

$$\Phi^{\mathrm{t}} \leqslant 0, \qquad \dot{\xi}\Phi^{\mathrm{t}} = 0, \qquad 0 \leqslant \xi \leqslant 1, \tag{22}$$

with the thermodynamic driving force, Π, given by

$$\Pi(\boldsymbol{\sigma}, T, \xi) = \boldsymbol{\Lambda}^{\mathrm{t}} : \boldsymbol{\sigma}^{\mathrm{eff}} + \frac{1}{2}\boldsymbol{\sigma} : \tilde{\boldsymbol{S}}\,\boldsymbol{\sigma} + \rho^{\mathrm{m}}\tilde{s}_0 T - \rho^{\mathrm{m}}\tilde{u}_0 - f^{\mathrm{t}}, \tag{23}$$

where $\tilde{s}_0$ and $\tilde{u}_0$ are the difference in reference entropy and internal energy, respectively between austenite and martensite. The constant Y^{t} is a critical value at which transformation occurs, a_1, a_2, and a_3 are transformation hardening coefficients, and n_1 ,..., n_4 are transformation hardening exponents. The parameters $\tilde{s}_0$, $\tilde{u}_0$, Y^{t}, a_1, a_2, and a_3 can all be expressed in terms of the phase diagram properties M_{s}, M_{f}, A_{s}, A_{f}, C^{A}, and C^{M} as shown in [57]. These material properties are to be determined and discussed in more detail later.

The constitutive equations must be further manipulated to determine the effects of the latent heat of phase change. The first law of thermodynamics (5) is expanded via (8b) as

$$\rho^{\mathrm{m}}\dot{u} = \boldsymbol{\sigma} : (\dot{\varepsilon}^{\mathrm{el}} + \boldsymbol{\alpha}\dot{T} + \boldsymbol{\Lambda}\dot{\xi}) + \boldsymbol{E}\cdot\boldsymbol{J} + \boldsymbol{E}\cdot\dot{\boldsymbol{D}} + \boldsymbol{H}\cdot\dot{\boldsymbol{B}} - \nabla\cdot\boldsymbol{q}. \tag{24}$$

A Legendre transformation is needed to combine and manipulate the Gibbs free energy and the first and second laws. This transformation is given by

$$\rho^{\mathrm{m}}u = \rho^{\mathrm{m}}G + \boldsymbol{\sigma} : \varepsilon + \rho^{\mathrm{m}}Ts. \tag{25}$$

Combining (24) and (25) gives

$$T\dot{s} = \frac{1}{\rho^{\mathrm{m}}}\Pi\dot{\xi} + \boldsymbol{E}\cdot\boldsymbol{J} - \nabla\cdot\boldsymbol{q}. \tag{26}$$

Now the definition of entropy is used to write

$$\begin{aligned}\boldsymbol{E}\cdot\boldsymbol{J} - \nabla\cdot\boldsymbol{q} = &-T\left(\frac{\partial^2 G}{\partial\boldsymbol{\sigma}\partial T}\dot{\boldsymbol{\sigma}} + \frac{\partial^2 G}{\partial T^2}\dot{T}\right)\\ &-\left[T\left(\frac{\partial^2 G}{\partial\xi\partial T} + \frac{\partial^2 G}{\partial\boldsymbol{\varepsilon}^{\mathrm{t}}\partial T}\boldsymbol{\Lambda}\right) + \frac{1}{\rho^{\mathrm{m}}}\Pi\right]\dot{\xi}\end{aligned} \tag{27}$$

in (27), $\dot{\xi}$ is eliminated using the fact that $\dot{\Pi} = 0$ during transformation [3], which yields

$$\dot{\xi} = \left(-\frac{\partial\Pi}{\partial\xi}\right)^{-1}\left(\frac{\partial\Pi}{\partial\boldsymbol{\sigma}}\dot{\boldsymbol{\sigma}} + \frac{\partial\Pi}{\partial T}\dot{T}\right). \tag{28}$$

substituting (28) reduces (27) to

$$\begin{aligned}\boldsymbol{E}\cdot\boldsymbol{J} - \nabla\cdot\boldsymbol{q} = &\left(\frac{1}{\rho^{\mathrm{m}}}\boldsymbol{\alpha}T - \mathfrak{D}\frac{\partial\Pi}{\partial\boldsymbol{\sigma}}\right):\dot{\boldsymbol{\sigma}}\\ &+\left(c - \mathfrak{D}\frac{\partial\Pi}{\partial T}\right)\dot{T}\end{aligned} \tag{29}$$

where $\mathfrak{D}$ is given by

$$\begin{aligned}\mathfrak{D} = &\left(-\frac{\partial\Pi}{\partial\xi}\right)^{-1}\\ &\times\left[\frac{1}{\rho^{\mathrm{m}}}\Pi - T\left(\frac{1}{\rho^{\mathrm{m}}}\tilde{\boldsymbol{\alpha}}:\boldsymbol{\sigma} + \tilde{c}\ln\left(\frac{T}{T_0}\right) + \tilde{s}_0\right)\right].\end{aligned} \tag{30}$$

If transformation is not occurring (i.e. $\dot{\xi} = 0$), (29) reduces to simply

$$\boldsymbol{E}\cdot\boldsymbol{J} - \nabla\cdot\boldsymbol{q} = \frac{T}{\rho^{\mathrm{m}}}\boldsymbol{\alpha}:\dot{\boldsymbol{\sigma}} + c\dot{T}. \tag{31}$$

2.3. Final field equations

The first governing equation combines linear momentum with Hooke's law and the strain-displacement relationship to give the Navier–Cauchy equations [50] written as

$$\nabla\cdot[\boldsymbol{C}(\nabla\boldsymbol{u} - \boldsymbol{\varepsilon}^{\mathrm{t}} - \boldsymbol{\alpha}(T - T_0))] = 0. \tag{32}$$

Assumptions are made to reduce the previous field and constitutive equations to simpler forms. First, we assume that the thermoelastic term $\boldsymbol{\alpha}:\dot{\boldsymbol{\sigma}}$ in the energy equation (31) is negligible. Furthermore, the effects of thermo–mechanical coupling due to latent heat are not modeled. Mirzaeifar *et al* [64] modeled the effects of latent heat on the response of SMA rods of circular cross section under pure torsion. A numerical method was used to solve the coupled energy and momentum equations. Tabesh *et al* [65] has also created a model which considers the effects of latent heat in a general 3D bodies, and this has been used in a the computational design optimization of 3D aerostructures [66]. The current work was undertaken to develop a finite element method that is applicable to arbitrary geometries with arbitrary distributions of Joule heating, which can have large gradients. To this effect, we simplify our model by neglecting the effects of latent heat and reduce (29) to

$$\frac{1}{2}\rho\boldsymbol{J}\cdot\boldsymbol{J} + k\nabla^2 T = c\dot{T}, \tag{33}$$

which is subject to the convection boundary condition given by

$$-k\frac{\partial T}{\partial\boldsymbol{n}} = h(T_{\mathrm{s}} - T_\infty), \tag{34}$$

where h is the convection coefficient, T_{s} is the surface temperature, T_∞ is the ambient temperature, and $\boldsymbol{n}$ is the unit normal to the boundary.

To reduce Maxwell's equations to a more useful form, we begin by combining Ampere's law with Ohm's law

$$\nabla\times\boldsymbol{H} = \nabla\times\left(\frac{1}{\rho}\boldsymbol{E}\right), \tag{35}$$

which can be rewritten as

$$\nabla(\nabla\cdot\boldsymbol{H}) - \nabla^2\boldsymbol{H} = \frac{1}{\rho}\nabla\times\boldsymbol{E} + \left(\nabla\frac{1}{\rho}\right)\times\boldsymbol{E}. \tag{36}$$

Now Gauss' law for magnetism and Farraday's law with (10a) can be combined to yield

$$\begin{aligned}\nabla^2\boldsymbol{H} = &\frac{\mu_0\mu_{\mathrm{r}}}{\rho}\frac{\partial\boldsymbol{H}}{\partial t} - \nabla\left(\boldsymbol{H}\frac{1}{\mu_{\mathrm{r}}}\nabla\mu_{\mathrm{r}}\right)\\ &-\rho\left(\nabla\frac{1}{\rho}\right)\times\nabla\times\boldsymbol{H},\end{aligned} \tag{37}$$

which can be reduced, assuming a homogeneous permeability and resistivity, to

$$\nabla^2\boldsymbol{H} = \frac{\mu_0\mu_{\mathrm{r}}}{\rho}\frac{\partial\boldsymbol{H}}{\partial t}. \tag{38}$$

Equation (38) is in the same form as the diffusion equation with constant coefficients, and is a common form in the induction heating literature. However this equation requires a boundary condition on the magnetic field, whereas the input to induction heating is usually the magnitude and frequency of the current in the coil. Therefore, we will derive an equation based on the current in the coil. To describe a vector field fully, both its divergence and curl must be uniquely defined. From Gauss' law for magnetism, the magnetic flux density has zero divergence such that it is represented by the curl of another vector $\boldsymbol{A}$ as

$$\boldsymbol{B} = \nabla\times\boldsymbol{A}, \tag{39}$$

where $\boldsymbol{A}$ is known as the magnetic vector potential. Now from Faraday's law, it follows that

$$\nabla\times\boldsymbol{E} = -\nabla\times\dot{\boldsymbol{A}} \tag{40}$$

or

$$\nabla\times(\boldsymbol{E} + \dot{\boldsymbol{A}}) = 0. \tag{41}$$

The curl of the gradient of any scalar field is always the zero vector (i.e. $\nabla\times(\nabla\phi) = \boldsymbol{0}$). This identity can now be applied

to the previous equation to give

$$\boldsymbol{E} = -\dot{\boldsymbol{A}} - \nabla\phi, \tag{42}$$

where ϕ is the electric scalar potential. Now substituting Ohm's law into Ampere's law gives

$$\nabla \times \boldsymbol{H} = \frac{1}{\rho}(-\dot{\boldsymbol{A}} - \nabla\phi), \tag{43}$$

into which the constitutive equation for $\boldsymbol{H}$ and the magnetic vector potential are substituted to yield

$$\nabla \times \nabla \times \frac{\boldsymbol{A}}{\mu_0\mu_r} = -1/\rho(\dot{\boldsymbol{A}} + \nabla\phi). \tag{44}$$

The source current is defined as $\boldsymbol{J}_s = -1/\rho\nabla\phi$. As is common in induction heating, we consider the excitation to be sinusoidal giving $\boldsymbol{A} = \boldsymbol{A}_0 e^{j\omega t}$ and $\dot{\boldsymbol{A}} = j\omega\boldsymbol{A}$, where $\boldsymbol{A}_0$ contains the magnitude and phase angle of $\boldsymbol{A}$. The same procedure can be done for $\boldsymbol{J}_s$ to give $\boldsymbol{J}_s = \boldsymbol{J}_{s0}e^{j\omega t}$. Combining the previous equations gives

$$\nabla \times \nabla \times \frac{\boldsymbol{A}_0 e^{j\omega t}}{\mu_0\mu_r} + \frac{j\omega}{\rho}\boldsymbol{A}_0 e^{j\omega t} = \boldsymbol{J}_{s0}e^{j\omega t}. \tag{45}$$

Assuming that the electromagnetic properties of the material do not vary spatially allows (46) to be rewritten as

$$\frac{1}{\mu_0\mu_r}\nabla \times \nabla \times \boldsymbol{A}_0 + \frac{j\omega}{\rho}\boldsymbol{A}_0 = \boldsymbol{J}_{s0}, \tag{46}$$

which is a more useful form than (38) and helps to formulate a much simpler weak form for the finite element implementation. The reason for using a form of the diffusion equation which considers a vector potential and current instead of magnetic field is for simplicity. The boundary conditions on the vector potential are simple because they decay to a small value far away from the workpiece such that the magnetic vector potential can be set equal to zero in the numerical implementation. The source current term $\boldsymbol{J}_{s0}$ in (46) corresponds to a simple current measurement. Now with the single measurement of a single input quantity and a sufficiently large finite element problem domain, we have defined the source term and the boundary conditions of the diffusion equation.

Returning to Ohm's law (10b) with the electric field written in terms of potentials we have

$$\boldsymbol{J} = -\frac{1}{\rho}\dot{\boldsymbol{A}} - \frac{1}{\rho}\nabla\phi = -\frac{1}{\rho}\dot{\boldsymbol{A}} + \boldsymbol{J}_s. \tag{47}$$

We now note that $\boldsymbol{J}$ has both source and induced current contributions expressed as

$$\boldsymbol{J} = \boldsymbol{J}_s + \boldsymbol{J}_e, \tag{48}$$

where the induced or eddy current is defined as

$$\boldsymbol{J}_{e0} = -\frac{j\omega}{\rho}\boldsymbol{A}_0 \tag{49}$$

and the minus sign indicates that the eddy currents are in the opposite direction relative to the source currents. The Joule heating term in (33) can now be reduced to a source term based on eddy currents [67] so that

$$\frac{1}{2}\rho\boldsymbol{J}_{e0}\cdot\boldsymbol{J}_{e0}^{*} + k\nabla^2 T = c\dot{T}, \tag{50}$$

where $\boldsymbol{J}_{e0}^{*}$ is the complex conjugate of $\boldsymbol{J}_{e0}$. Note that $\boldsymbol{J}_{e0}\cdot\boldsymbol{J}_{e0}^{*}$ is equivalent to $|\boldsymbol{J}_{e0}|^2$. When writing (33), no assumption was made regarding the form of $\boldsymbol{J}$. But we have now assumed that the current density and therefore the eddy current density is harmonic and thus has real and imaginary parts. Therefore, the complex conjugate must be used in order to account for both the real and imaginary parts of $\boldsymbol{J}_{e0}$. In writing the Joule heating term solely as a function of $\boldsymbol{J}_{e0}$, it is assumed that heating due to electromagnetic hysteresis is negligible compared to eddy currents and that there is no source current applied in the workpiece. Thus with the rate of Joule heating known the remaining thermo–mechanical equations can be solved.

2.4. Model implementation

The governing electromagnetic equation (equation (46)) is implemented in Abaqus Unified FEA [68]. The SMA constitutive behavior captured in section 2.2 is also implemented in Abaqus via a user material subroutine [69, 70]. In solving the coupled electromagnetic thermo–mechanical problem of induction heating of SMA components, it is assumed that the problem is one-way coupled and can be solved sequentially; specifically, the electromagnetic problem is solved for a given geometry and input coil current, after which the thermo–mechanical problem is solved considering the generated volumetric heat sources and hysteretic SMA constitutive behavior. This process is similar to the one used by Bay *et al* in [71] on non-transforming materials. In that work, a numerical model was created which considered the thermoelastic-plastic behavior of an axisymmetric workpiece being inductively heated including the variation in magnetic material properties with very large changes in temperature. Here we assume relatively small temperature changes such that the resistivity and magnetic permeability do not vary with temperature. This assumption allows us to eliminate feedback so that the process can be simplified to a one-way (feedforward only) process as illustrated in figure 1.

In the overall engineering model, the coil is assumed to be tightly wound so that it can be considered a continuous sheet. A consequence of this assumption is that the phase angle between the applied current and voltage is assumed to be strictly 90° (i.e there is no lag in the voltage and current in time). In an experimental setup a tightly packed coil is typically desired to achieve maximum current density (i.e. faster heating) and a uniform heating distribution along the length of the workpiece. In addition to the model description of the workpiece and coil geometry, one must consider the domain of air or vacuum around the workpiece. In this work, the initial size of the problem domain is chosen based on the recommendation given in [68] as approximately ten times the characteristic length scale of the coil and workpiece. In particular, the outer dimension of the domain was chosen such that the field intensity at its boundary was two orders of

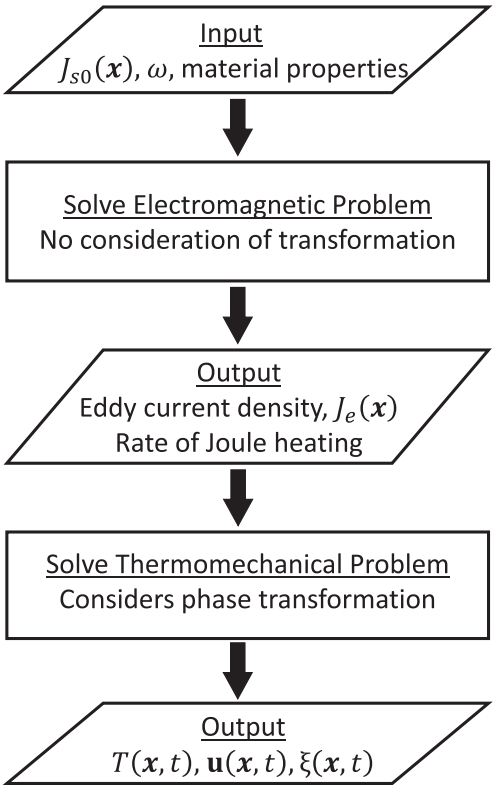

Figure 1. Induction heating model flow process.

magnitude less than the field intensity at the point of highest field. The finite element mesh in this domain is globally refined until a converged solution is found then we coarsen the global mesh with local refinements where high gradients exist so that the number of elements, and corresponding analysis time, is reduced while maintaining solution accuracy. In the electromagnetic problem, a body current density ($\boldsymbol{J}_{s0}$) and frequency are applied in the coil and null magnetic vector potential boundary conditions are applied on the outer domain ($\boldsymbol{A}_0 = 0$). The only electromagnetic material properties required and considered in this implementation are electrical resistivity and magnetic permeability. The coil is modeled as an equivalent current sheet in space, not as an actual material therefor, the resistivity and permeability are considered the same as vacuum to prevent calculation of eddy currents in the coil [49, 67]. In some electromagnetic modeling implementations, the proposed form of Ohm's law is piece-wise so that $\boldsymbol{J} = 0$ outside of the conducting workpiece [71]. The effects of a piece-wise form of Ohm's law and assuming properties of vacuum in the coil have the same effect, which is numerically preventing eddy currents from being solved in the coil, which is being modeled as only an equivalent current sheet. From the electromagnetic analysis, the nodal location and magnitude of the Joule heating rate are obtained and mapped into the thermo–mechanical problem as a volumetric heat source. This numerical results extraction and mapping is performed using a Python script, which is able to extract the required information from the analysis output files.

The thermo–mechanical problem considers the transformation of the SMA component being heated via a volumetric heat source with convective boundary conditions on all SMA surfaces except where the coil is located. The model does not consider thermal conduction or radiation from the coil. This is because experimental measurements have shown that the coil temperature is approximately equal to the SMA surface temperature throughout the heating process. An adiabatic boundary condition is then assumed in place of modeling convection at the coil surface or the conduction and radiation between the SMA body and the coil. The outputs of the thermomechanical analysis include the temperature and displacement fields as well as the martensitic volume fraction throughout the SMA piece.

3. SMA material constant determination

Calibration of the SMA material properties is required to ensure the accuracy of the model. The calibration was performed in two stages: the electromagnetic stage and the thermo–mechanical constitutive stage.

3.1. Electromagnetic constants

As discussed in section 2.3, the only material properties required to model the electromagnetic behavior of the SMA are the electrical resistivity and magnetic permeability. Experimental measurements showed that the relative permeability of NiTi is approximately 1.002 in either phase, which is also observed in the literature [72]. The experiments showed that the SMA resistivity is 76 $\mu\Omega\,\mathrm{cm}^{-1}$ in austenite and 82 $\mu\Omega\,\mathrm{cm}^{-1}$ in martensite. For the sequentially coupled (feedforward) approach, it is not feasible to change the resistivity with phase changes. Therefore, a single constant resistivity of 80 $\mu\Omega\,\mathrm{cm}^{-1}$ was chosen[4].

3.2. Thermomechanical constants

The constitutive model was calibrated using experiments performed on a homogeneous, prismatic tube with length L of 8 in. (203 mm) with outer d_o and inner d_i diameters of 0.375 in. (9.525 mm) and 0.225 in. (5.715 mm), respectively. To determine the material constants, the tube was subjected to thermal cycles under different constant torques. The tube is fixed at one end (zero displacement) and has an applied twisting moment at the opposite end (applied traction). The lateral surfaces of the tube are traction free. The temperature is spatially uniform and varies from below the martentsite finish temperature to above the austenite finish temperature. The torque T and free end rotation angle θ were measured in the experiment. The torque was then converted to shear stress

[4] Choosing this intermediate resistivity gave a Joule heating rate that was 6% different than the purely austenite value and 3% different than the purely martensite value. The difference in the rate of Joule heating of pure martensite or austenite was 9%.

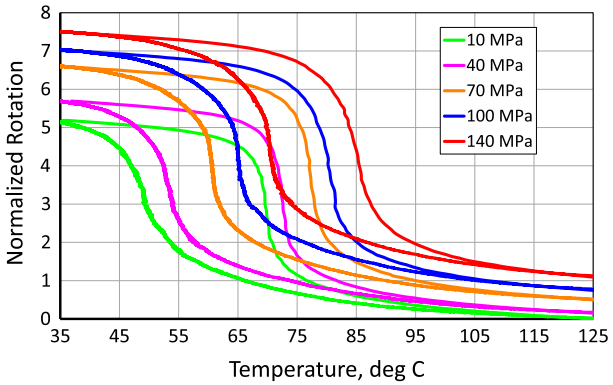

Figure 2. Experimental normalized rotation-temperature diagram for torsional loading of a NiTi tube ($d_o = 9.525$ mm, $d_i = 5.715$ mm) corresponding to approximately 1, 5, 9, 13, 18.5 Nm of applied torque.

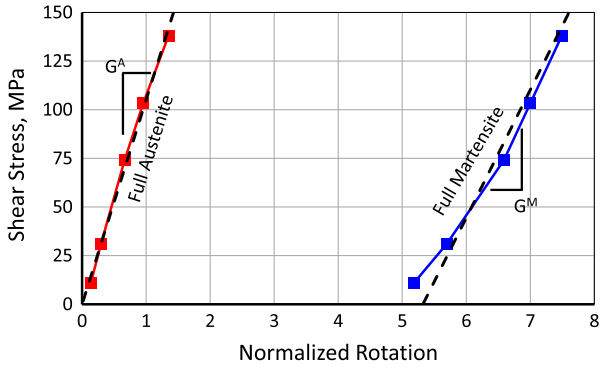

Figure 3. SMA tube dynamic modulus measurements correspond to figure 2 with linear fit. The modulus in martensite depends on the amount of transformation strain the SMA has developed but in highly trained tubes $H^{\mathrm{cur}}(\bar{\sigma}^{\mathrm{eff}}) \approx H_{\max}$.

to be compatible with the FEA outputs by

$$\sigma_{23} = \sigma_{32} = \tau = \frac{Td_o}{2J}, \tag{51}$$

where τ is the shear stress at the outer surface of the tube, and J is the second moment of area given for hollow tubes as $\frac{\pi}{32}[d_o^4 - d_i^4]$ [50]. The rotation angle throughout this work is normalized by a diameter to length ratio $d_o/(2L)$. The normalized rotation-temperature curves generated by this experiment following the conversion from torque to shear stress and normalizing rotation are shown in figure 2, which is used for the remainder of the thermo–mechanical material constant determination. The temperature in the experiment was measured by a thermocouple placed on the outer surface of the tube at the mid-length. During these experiments, induction heating was used to transform the SMA tube[5].

The first step in determining the material constants is to consider the thermo-elastic response, which provides the austenite and martensite elastic moduli, Poisson ratios, and thermal expansion coefficients. The austenite and martensite Poisson ratios are assumed to be equal and constant as is common in macro-scale SMA modeling. The thermal expansion response is taken to be isotropic. To determine the elastic modulii, the shear stress and strain were read from figure 2 for each loading when the tube is completely austenite and martensite and then plotted to create what has been referred to as the dynamic modulus [12], shown in figure 3. Assuming a perfectly trained material, the strain in austenite is purely elastic so that the shear modulus G can easily be measured as the slope of the fit to the austenite line in figure 3. The modulus in martensite depends on the amount of transformation strain the SMA has developed. However, for this highly trained tube the behavior is close to linear so that we can approximate the martensite shear modulus in the same manner as the austenite modulus. The shear modulii for the tube as measured from figure 3 are then used to calculated to the elastic modulii by $E = 2(1 + \nu)G$.

[5] The frequency in the induction system was such that the thermal gradients in throughout the tube were small and when the results are compared to more conventional and thermally uniform conductive heating, there is no significant difference.

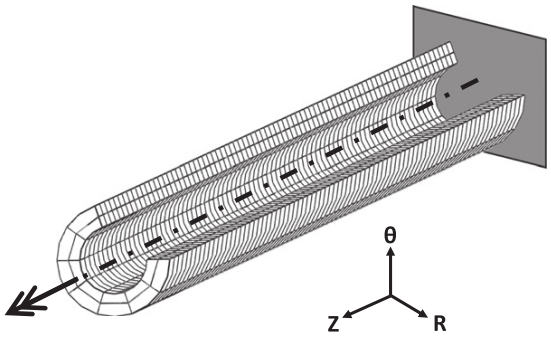

Figure 4. Finite element model created to determine the SMA transformation constants. One quarter of the model is cut away for detail.

The transformation constants are divided into three categories: the phase diagram parameters, the transformation strain parameters, and the smooth hardening parameters. The smooth hardening parameters, $n_1 \ldots n_4$, can be tuned in the range $0 < n_i \leqslant 1$ to approximate 'smoothness' of the transformation hysteresis. The phase diagram parameters that must be determined are the martensite and austenite start and finish temperatures (M_s, M_f, A_s, A_f) and martensite and austenite stress influence coefficients (C^M, C^A) [57]. The transformation strain parameters include the maximum transformation strain (H_{Max}), the back stress tensor ($\boldsymbol{\beta}$), and k^t. For the case of a torque tube, $\boldsymbol{\beta}$ is taken to be a single non-zero component such that $\beta_{ij} = \beta\delta_{i2}\delta_{j3}$, where δ_{ij} represents the second-order identity tensor and the 2–3 (θ–Z) direction corresponds to torsion about the longitudinal axis (see figure 4).

A first-order approximation was made for the phase diagram properties simply by inspection of figure 2, and the initial smooth hardening and transformation strain parameters were found in the literature [14]. Finding the material constants in this manner generally gives a model that is approximate but does not capture the full behavior of the SMA. To refine the parameters, a finite element model of the test was constructed, as shown in figure 4. In this model the

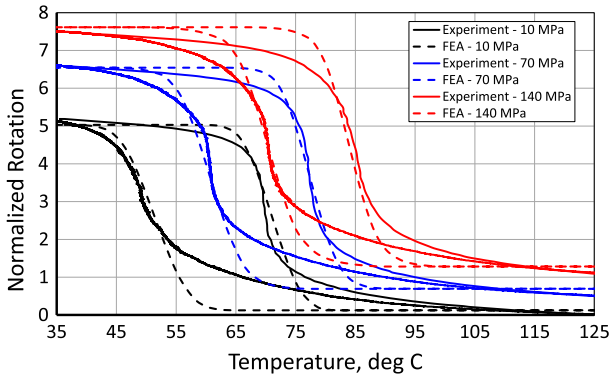

Figure 5. Comparison of experimental and calibrated finite element strain-temperature diagrams.

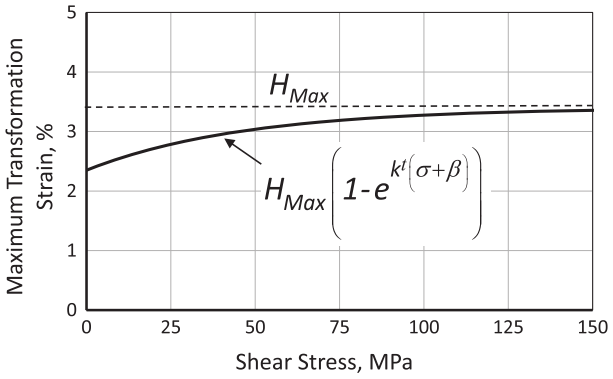

Figure 6. Maximum transformation strain achievable in the tube ($H_{\max} = 3.35\%$, $k^{\mathrm{t}} = 0.0172\ \mathrm{MPa}^{-1}$, and $\beta = 58$ MPa) at a given shear stress σ.

geometry, loading, and boundary conditions match the test setup so that only the transformation constants are varied to match the experiment data. The model consists of 1600 three-dimensional quadratic reduced integration brick elements (Abaqus designation C3D20R).

While an optimization would be the most accurate way to determine the constants by minimizing the error between the model and experiment, the process to set up an optimization is beyond the scope of this work, which is intended to focus more on the thermal behavior of the SMA rather than the accuracy of the mechanical transformation behavior. The final result of the approximated calibration is shown in figure 5 with figure 6 showing the transformation strain parameters. As can be seen in figure 6, the maximum transformation strain does not change significantly, which aids in verifying the assumption used in determining the martensite shear modulus. The result of the calibrations are summarized in table 2. These parameters are used when modeling the SMA tube. No experiments were performed to calibrate the SMA beam material properties used in section 4.2 as no associated experimental study of inductively heated SMA beams has been performed. Instead, properties were taken directly from [17]. The beam properties are also summarized in table 2.

Table 2. SMA electromagnetic, thermal, and mechanical constitutive material parameters.

Parameter	Tube	Beam[a]
(Electromagnetic parameters)		
μ_{r}	1.002	1.002
ρ ($\mu\Omega$ cm^{-1})	80	80
(Heat transfer parameters)		
ρ^{m} (kg m^{-3})	6450	6450
c (J kg^{-1} K^{-1})	400	400
k (W m^{-1} K^{-1})	10	10
(Thermoelastic parameters)		
E^{A} (GPa)	27.98[b]	90.0
E^{M} (GPa)	17.49[b]	63.0
$\nu^{\mathrm{M}} = \nu^{\mathrm{A}}$	0.33	0.33
$\alpha^{\mathrm{M}} = \alpha^{\mathrm{A}}$ (K^{-1})	0.00	10×10^{-6}
(Phase diagram parameters)		
M_{s}, M_{f} (K)	335, 311	295, 280
A_{s}, A_{f} (K)	333, 354	353, 362
C^{M}, C^{A} (MPa K^{-1})	5.5, 7.9	5, 10
(Transformation parameters)		
H_{Max} (%)	3.35	6.0
k^{t} (MPa^{-1})	0.0172	0.00752
β (MPa)	58	0.0
(Smooth hardening parameters)		
$n_{1,2,3,4}$	0.3	0.35

[a] After [17], where applicable.
[b] Calibrated from torsion testing.

4. Results and discussion

The applications presented herein include SMA tubes that exhibit a two-way SME that induces twisting about the longitudinal axis and one-way SMA beams that bend during actuation.

4.1. SMA torque tube

The tube in this study is the same that is described in section 3 and is shown with an idealized (i.e. homogenized) coil model in figure 7. The analysis of the tube is completed in two stages as previously described. For the electromagnetic analysis the entire domain, including the coil and tube, is meshed with 50 190 electromagnetic linear hexahedral electromagnetic elements (Abaqus designation EMC3D8); the mesh is concentrated through the thickness of the SMA tube where gradients are highest and of most interest. In the thermo–mechanical portion of the analysis only the tube is modeled using 4370 linear hexahedral temperature-displacement elements with reduced integration (Abaqus designation C3D8RT). The thermo–mechanical model is similar to that

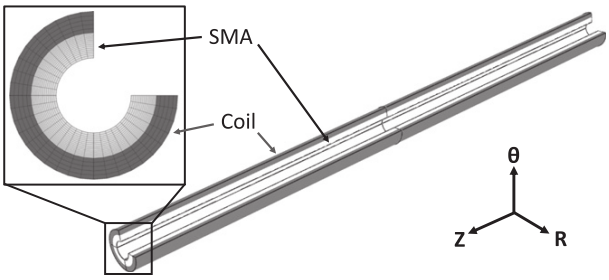

Figure 7. Electromagnetic FEA model of the SMA torque tube with the vacuum domain omitted. One quarter of the model is cut away for visualization. The mesh through the thickness is shown enlarged for detail.

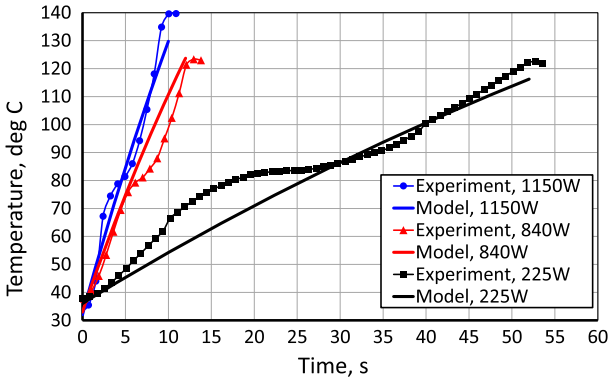

Figure 8. Power measurement study results. The highest heating rates correspond to the highest input power.

shown in figure 4 with a more refined mesh. The refined mesh accommodates mapping of the Joule heating field from the electromagnetic result to each element in the thermo–mechanical model and helps to better capture thermal gradients.

Two experimental tests of this tube are simulated and compared to the model. The first is an input study where the power into the induction coil is varied to determine how the developed model compares to various inputs. The second study is a high rate actuation test to verify the behavior of the model at a relatively small time scale. A final test of the model is simulated but not completed experimentally, which shows the effects of a changing frequency on the variation of temperature, shear stress, and martensite volume fraction through the tubes wall thickness.

4.1.1. Power variation study. In the first study, the input power to the experimental induction system is varied and the temperature at the middle of the tube on the outer surface is measured. The power is varied by maintaining a constant frequency and varying the coil current across three levels. The three input RMS coil currents are 49.9 A, 45.3 A, and 21.4 A at a frequency of 55 kHz, which correspond to power levels of 1150 W, 840 W, and 225 W respectively. By treating the induction system as a transformer, the impedance can be found. This allows a real power in the coil to be found. The real coil power is the power which contributes to the heating of the SMA and coil. It is assumed that the coil is not being heated so that all of the power is transferred into the SMA. The real coil powers produced were found to be 488 W, 417 W, and 135 W and correspond to input powers of 1150 W, 840 W, and 225 W respectively. The real coil power, which assumed to be completely transferred to the SMA body, agrees well with the power found through the FE model. The temperature is measured by a non-conductive type K thermocouple. The study uses a 10 AWG copper magnet wire wrapped tightly around the SMA tube. There is no cooling in this scenario to minimize the number of possible variables in the experiment. In this study only the heating of the tube is modeled since cooling is accomplished by free convection over a long time relative to heating. The torque in all 3 experiments was held constant at 21 Nm. The results of the experiment and model are shown in figure 8. The model agrees with the experimentally measured temperature within 15% at all times. The largest discrepancies between the model and the experiment are due to the effects of the latent heat of phase transformation, which are not considered in the model. The latent heat is manifest as significant deviations from linearity in figure 8.

In section 1, it was noted that resistive heating large SMA components like torque tubes is limited by current. To show this qualitatively, the power measures in the previous experiments is used in a simple resistive heating calculation given as

$$P = I^2 \rho \frac{L}{A}, \tag{52}$$

where P is the power, I is the DC current, ρ is the resistivity (taken to be 80 $\mu\Omega$ cm), L is the length, and A is the cross sectional area of the tube ($\frac{\pi}{4}[d_e^2 - d_i^2]$). For the particular tube implemented this can be reduced to $P = 3.56 \times 10^{-3} I^2$. The DC current I needed to generate an equivalent power to the induction system can now be solved for 488 W, 417 W, and 135 W as 370 A, 342 A, and 195 A respectively. These currents are significantly higher than current of 49.9 A, 45.3 A, and 21.4 A used in the induction system, demonstrating why resistive heating can be difficult to achieve in large pieces.

4.1.2. High rate actuation study. With the ability of the model to match experimental results demonstrated, a second study was complete to achieve high rate actuation in the SMA tube. In this second study, the high rate heating was achieved by changing from a 10 AWG coil to a smaller 14 AWG coil to increase the coil current density. In the induction coil an RMS current of 33 A and voltage 31.5 V were applied at 49.1 kHz. The applied torque again remained constant at 21 Nm. To achieve high rate cooling, active cooling was implemented by flowing a mixture of 90% water and 10% ethylene glycol at a volumetric flow rate of 1.2 gal min^{-1} (75 cm^3 s^{-1}) through the tube. During heating this mixture was stationary in the tube. A diagram of this cooling setup is shown in figure 9 where the coil is omitted. The extra components to accommodate coolant flow were not included

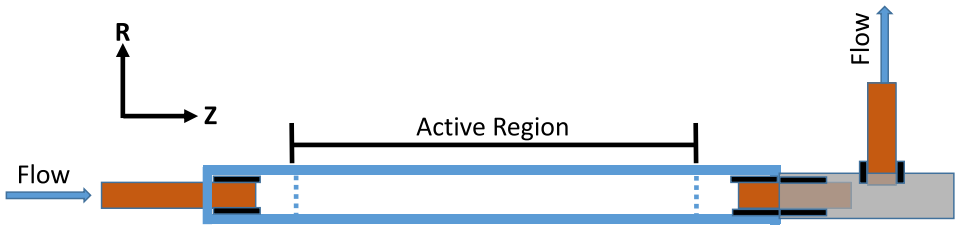

Figure 9. SMA tube diagram for coolant flow.

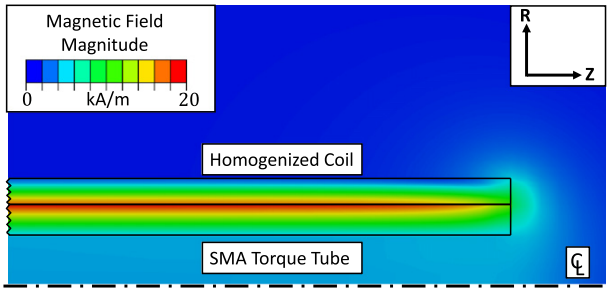

(a) Magnetic field magnitude

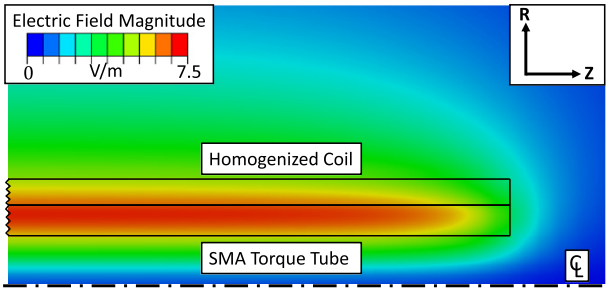

(b) Electric field magnitude

Figure 10. Induced time harmonic electromagnetic field magnitudes in the SMA and surrounding domain for the high rate actuation study.

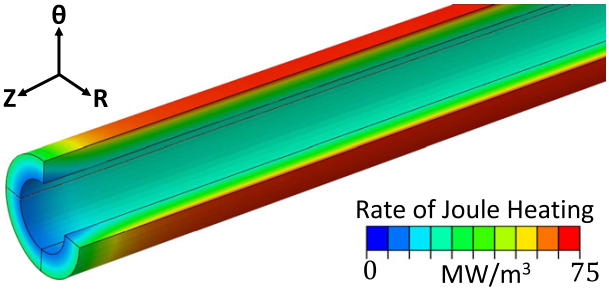

Figure 11. Rate of Joule heating induced in the SMA due to the time harmonic electromagnetic fields of figure 10 during the high rate actuation study.

in the model and only the active portion of the tube is considered. The thermal effect of the flow was simulated using a convection boundary condition.

The magnetic and electric fields induced in the high rate actuation study are shown in figure 10, where the end portion of the tube is shown in particular as the fields become uniform

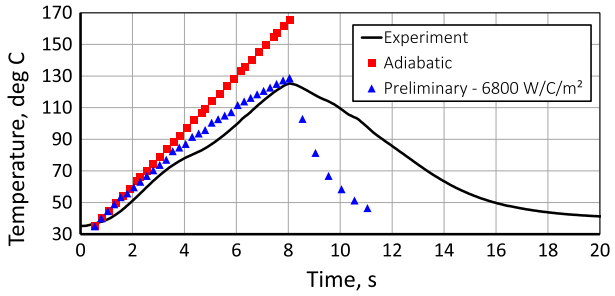

Figure 12. Temperature response of the SMA tube in the high rate actuation study with calculated convection coefficient. The experiment data is compared to adiabatic conditions and calculated convection conditions.

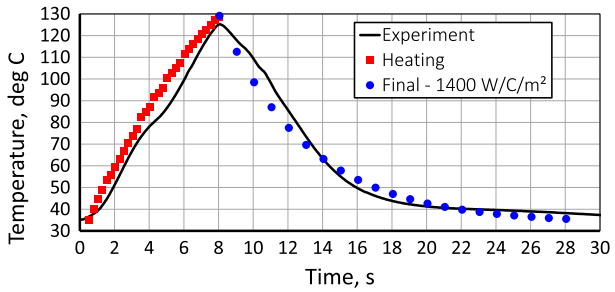

Figure 13. High rate actuation experiment compared to FEA results. Convection coefficient found through a parametric study.

away from the ends. The ability to visualize these fields both inside and outside of the SMA helps in understanding possible consequence arising from the generation of a free magnetic or electric field in a system that involves other electronics.

The rate of Joule heating induced by eddy currents in the tube is shown in figure 11 and is a result of the electromagnetic fields from figure 10. All fields show a distinct end effect which lowers the overall heating rate of the system; in the case shown the effect on the overall heating rate is small.

During heating, a free convection condition boundary condition was used to model the stationary water. This result was compared to an adiabatic case in figure 12 so the effects of the stationary water in the tube during heating are made more apparent. During cooling, we must calculate a convection coefficient from analytical solutions or use a fluid dynamics analysis. The latter is beyond the scope of this work. Rather, we choose to calculate an effective convection

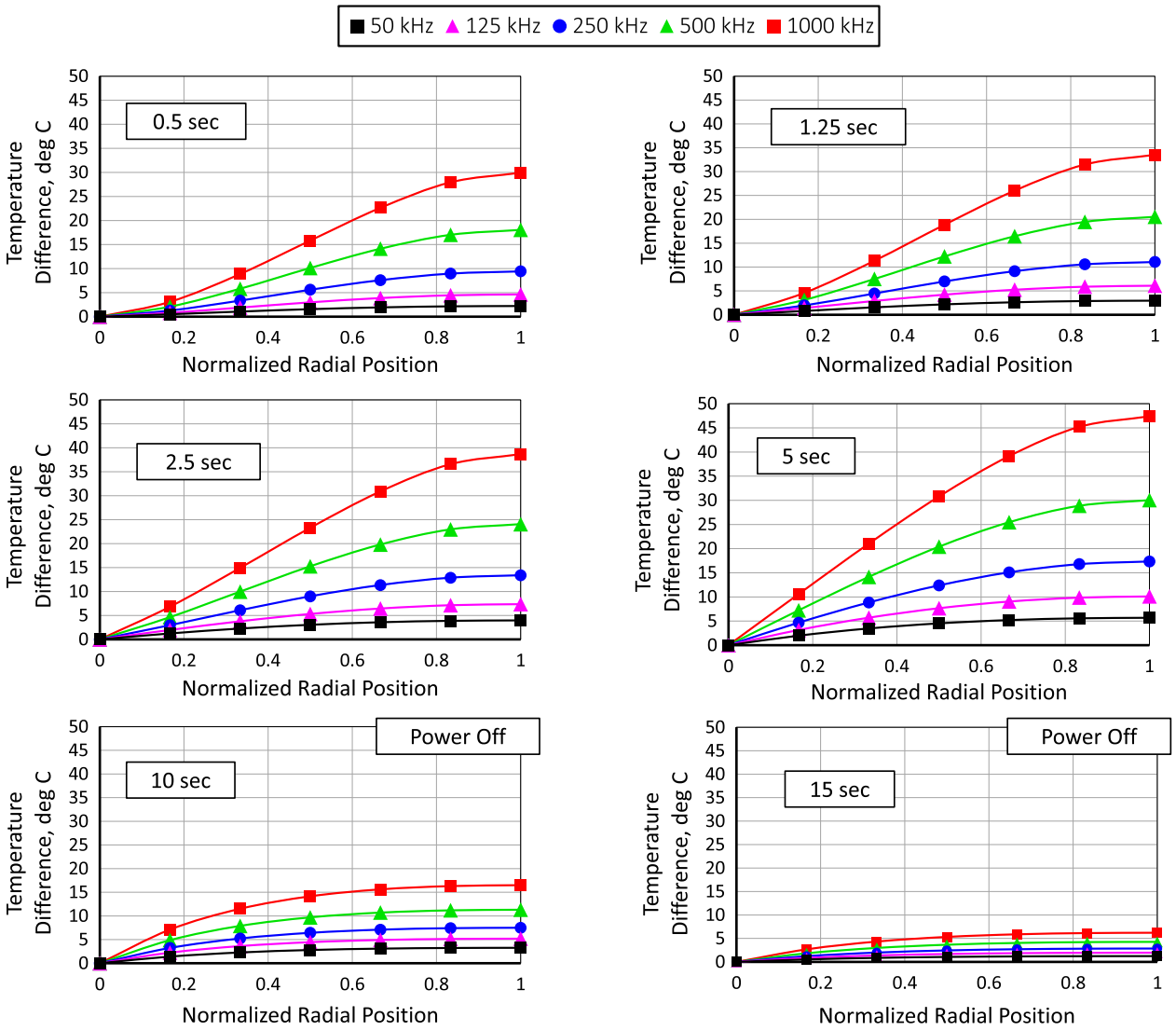

Figure 14. Temperature distribution at varying frequencies and a constant loading. The normalized radial position corresponds 0 at the inner surface of the tube and 1 at the outer surface. The temperature difference is measured relative to the temperature at the inner surface. Heating for 5 s using a 14 AWG coil with RMS current of 35 A followed by active flow cooling using the results of the high rate actuation study.

coefficient. The result of this calculation is shown in figure 12 and further calculation details are discussed in appendix.

The result of the calculated convection coefficient is not in good agreement with the experiment so a parametric study was completed to determine a convection coefficient that could describe the cooling process. The result of this study is shown in figure 13 and described in more detail in appendix.

4.1.3. Frequency variation effects. In the two previous studies, the developed model has proven to be accurate during the heating of the tube and with some manipulation is able to analyze cooling also. We now use this model to analyze the effects of changing the frequency, and therefore Joule heating distribution, in the SMA tube. Such a capability will enable future analysis driven design. In this study, we subject the tube to a constant 13 Nm torque then heat for 5 s using a 14 AWG coil with RMS current of 35 A. The tube is cooled for 20 s using the same active cooling scenario demonstrated in section 4.1.2. The purpose of this study is to visualize the effects of a changing induction frequency on the radial distributions of temperature, martensite volume fraction, and shear stress. It is important to note that this is a purely numerical predictive investigation and no experiments have been performed. Also note that the higher frequencies produce a higher overall temperature in the tube than do lower frequencies at the same current. This leads to a difference in the cooling behavior between each frequency where the lower frequencies cool and transform before the higher frequencies.

The radial temperature distributions in time are shown in figure 14 with the corresponding martensite volume fractions and shear stresses shown in figures 15 and 16 respectively. In

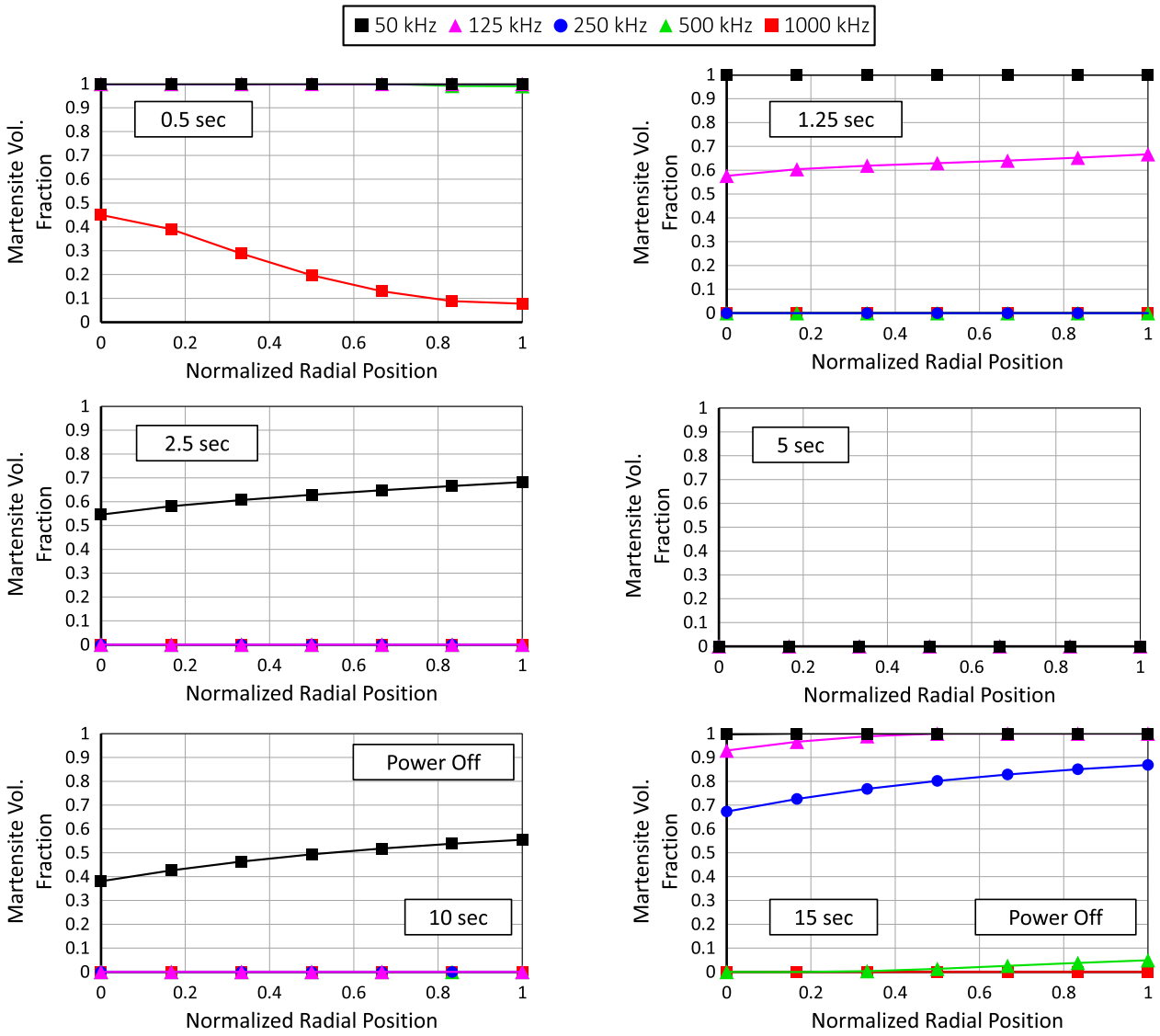

Figure 15. Martensite volume fraction profile through the tube thickness at various frequencies and a constant loading. Heating for 5 s using a 14 AWG coil with RMS current of 35 A followed by active flow cooling using the results of the high rate actuation study.

these figures the normalized radial position corresponds to 0 at the inner surface of the tube and 1 at the outer surface. Due to the skin effect of (1), the radial temperature gradient is more pronounced at higher frequencies.

This temperature variation with frequency is then manifest in the distributions of martensite volume fraction during heating as the higher frequencies lead to earlier transformation during heating and delayed transformation during cooling. The skin depth effect at high frequencies also causes a strong gradient in the evolution of martensite through the radius of the tube. For lower frequencies, the radial temperature gradient is small and the shear stress before transformation varies approximately linearly in the radial direction, as expected in tubes. Therefore, the martensite evolves approximately linear in the radial direction. However, for higher frequencies, the higher radial temperature gradients cause a highly nonlinear behavior that can, to some extent, be controlled by the magnitude and frequency of the coil current. This controlability provides new possibilities for optimizing the actuation systems for particular applications (e.g. increasing fatigue life, optimizing training procedures, etc.). Note in particular the case of 1000 kHz, where a θ–Z shear stress increase of 70 MPa over the nominal as loaded stress of 88 MPa is observed. In addition to the large θ–Z shear stress gradient at 1000 kHz, there is also a small but noticeable predicted increase in R–θ shear stress gradient. The difference in the maximum and minimum R–θ shear stress changes from approximately 1 MPa in the low frequency cases to about 5 MPa in the 1000 kHz case.

4.2. SMA beam

As a demonstration of generality and to guide future development efforts, an SMA beam heated by a planar induction

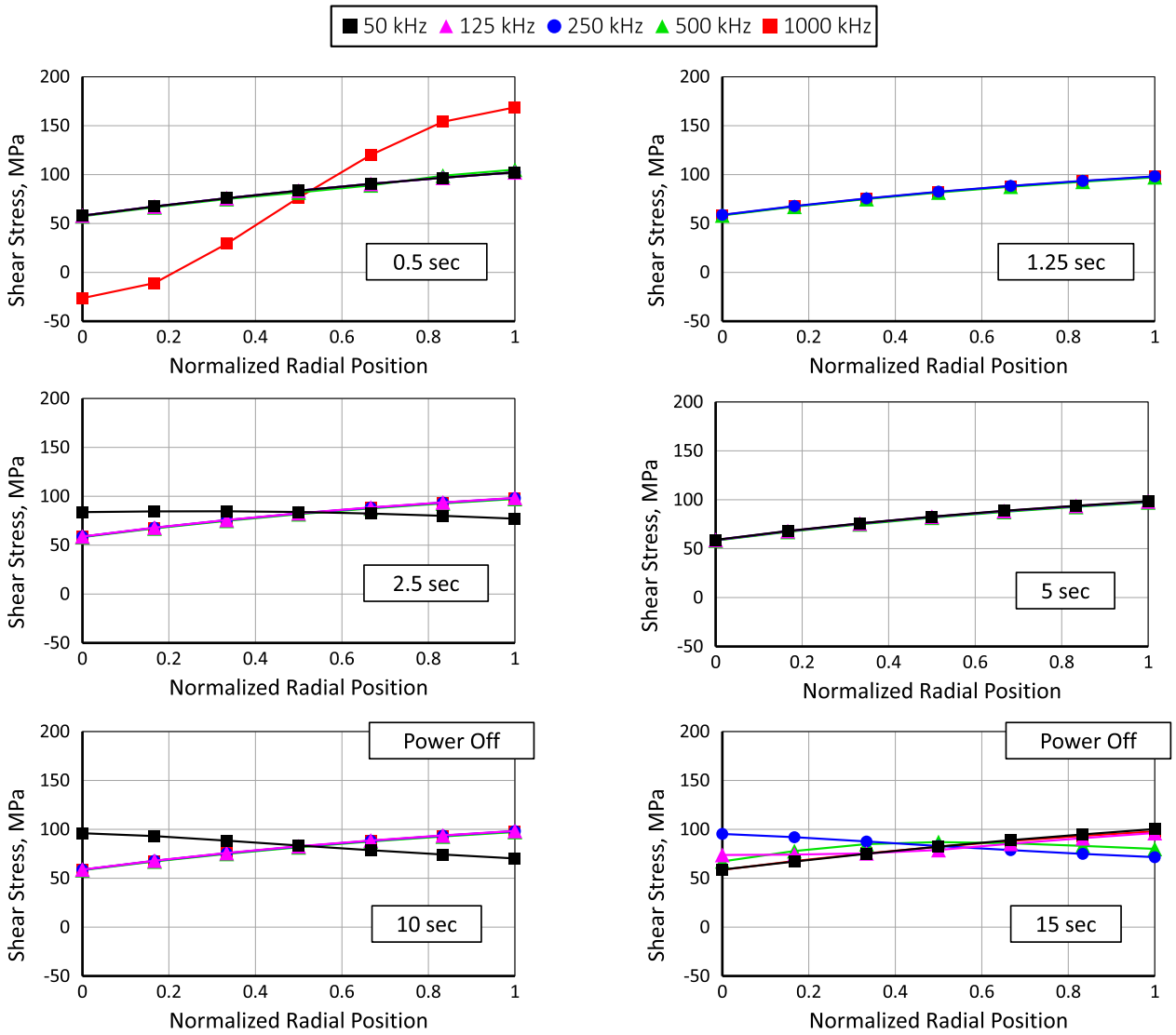

Figure 16. θ–Z shear stress profile through the tube thickness at various frequencies and a constant loading. Heating for 5 s using a 14 AWG coil with RMS current of 35 A followed by active flow cooling using the results of the high rate actuation study.

coil was likewise simulated but was not experimentally studied. A planar coil is the configuration used in induction cook tops [73]. The RMS coil current and frequency considered are 40 A and 55 kHz, respectively. The SMA beam has length of 5 in. (127 mm), a width of 1.5 in. (38.0 mm), and a thickness of 0.2 in. (5.1 mm). The outer diameter of the coil is equal to the width of the SMA beam, with 12 turns of 20 AWG copper wire. The homogenized coil on the SMA beam is shown in figure 17(a) and, as before, is taken to be a homogenized current sheet rather than being composed of individual coil turns. The coil is placed at the fixed end of the beam. The free end of the beam has a constant force of 75 N applied orthogonal to the beam axis and in the direction of the beam short dimension. As another example, a rectangular planar coil with the same input current, width, and 20 AWG wire as the circular coil is considered, where the length is 2 in. (50.8 mm) and only 4 turns of wire are considered as shown in figure 18. The Joule heating rate and maximum temperature at 5 s are significantly lower than in the beam with a circular coil, but the final displacement (referred to as the loaded cool condition) is the same, as shown in figure 19. Note that the circular coil produces lower temperature zones in the corners of the beam, which are absent for the rectangular coil. These lower temperature zones do not reach transformation and cause only a portion of the beam to actuate. This leads to stress concentrations that are not seen with the rectangular coil. This result motivates future work focusing on detailed design optimization of the coupled actuator/coil configuration.

4.3. Flux concentrators

In induction heating, it is common to introduce a body made of high permeability, high resistivity material into the system in close proximity to the induction coil. Such a body is known

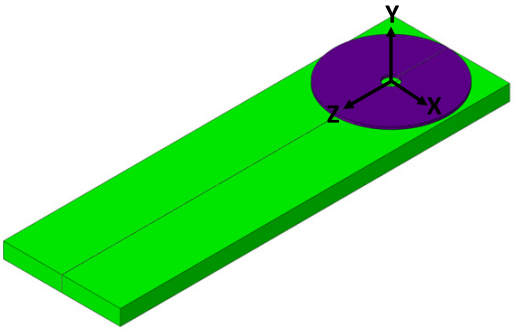

(a) SMA beam with circular coil geometry.

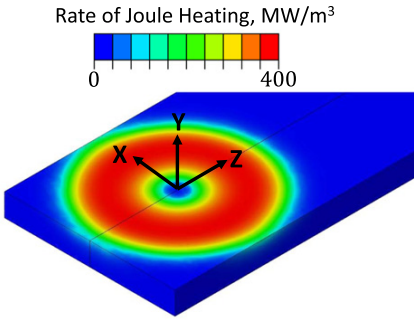

(b) Rate of Joule heating produced in the SMA by the circular coil.

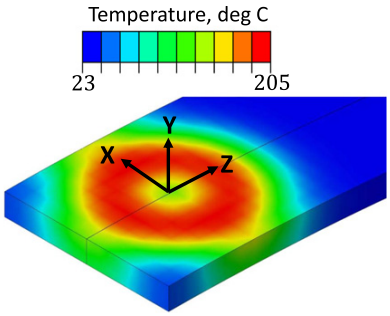

(c) Corresponding temperature profile in the SMA beam.

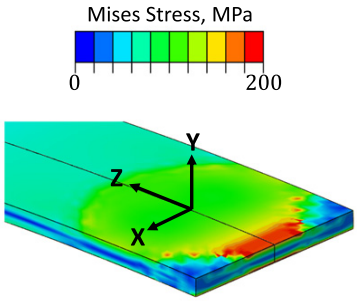

(d) Mises stress profile in the SMA beam due to a constant force of 75 N applied orthogonal to the beam axis and in the direction of the beam short dimension.

Figure 17. Homogenized 12 turn 20 AWG circular coil on an SMA beam. The beam is heated for 5 s using an RMS current of 40 A at 55 kHz.

as a magnetic flux concentrator (MFC) (also called flux intensifier, diverter, or controller) [52]. The effect of this MFC is to locally increase the intensity of the magnetic fields near the workpiece and prevent the spread of electromagnetic power that otherwise would not contribute to heating the workpiece [52]. The local increases in magnetic field lead to increased electrical efficiency and heating rate [74]. MFCs are commonly made of magnetic alloy laminations, magneto-dielectrics [75], or ferritic materials [76], where each has specific advantages and disadvantages and can be configured to work best in a specific frequency range. To study the effects of these MFCs, we model a 0.5 mm thick solid disk concentrator made of NiZn ferrite [77–79], placed above the circular coil model previously described. The NiZn ferrite can have large variations in material properties; for this work we use a relative magnetic permeability of 1500 and a resistivity of 10^7 Ω cm [79]. No inputs to the system or dimensions were changed from the analysis that generated figure 17. The results shown in figure 20 indicate a dramatic increase in heating rate relative to the case without a flux concentrator. This finding clearly motivates the use of flux concentrators in the induction system and shows that they should be further studied and incorporated into future design optimization.

5. Conclusions and future work

Custom SMA actuators can be best designed given an in-depth knowledge of the internal temperature, stress, and martensitic volume fractions as functions of space and time. This work established a new analysis tool for simulating induction heating of arbitrarily shaped monolithic SMA components and systems that implement them. The model developed has been validated and verified against experiments. The verification showed that the model could accurately predict the temperature response of an SMA tube given various frequency and current inputs for cases with and without active cooling. Additional modeling efforts showed that the distribution of temperature, stress, and martensite volume fraction could be controlled by changing the frequency of the input current. Further control of the distribution and magnitude of the electromagnetic fields in and around the SMA workpiece can also be achieved by employing a MFC, which can substantially increase heating/actuation rate.

Future work will focus on using the model to improve actuation systems incorporating inductively heated SMA tubes and beams. Such actuation systems can only realize their peak performance in terms of actuation rate, only if the SMA actuator, induction system, flux concentrators, cooling

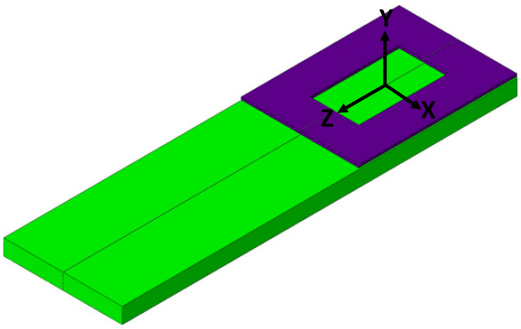

(a) SMA beam with rectangular coil geometry.

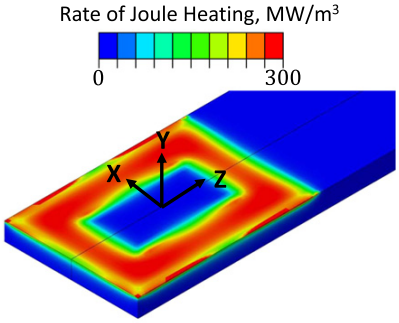

(b) Rate of Joule heating produced in the SMA by the rectangular coil.

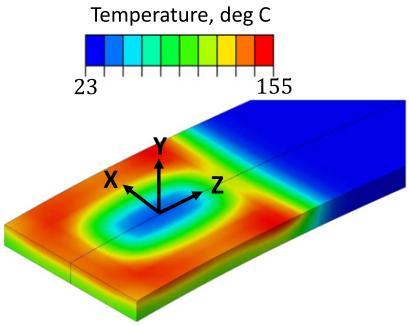

(c) Corresponding temperature profile in the SMA beam.

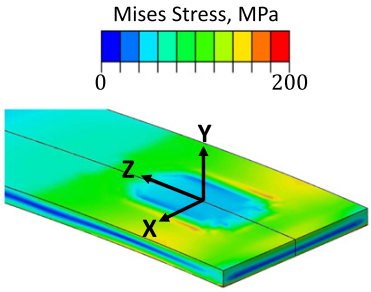

(d) Mises stress profile in the SMA beam due to a constant force of 75 N applied orthogonal to the beam axis and in the direction of the beam short dimension.

Figure 18. Homogenized 4 turn 20 AWG rectangular coil on an SMA beam. The beam is heated for 5 s using an RMS current of 40 A at 55 kHz.

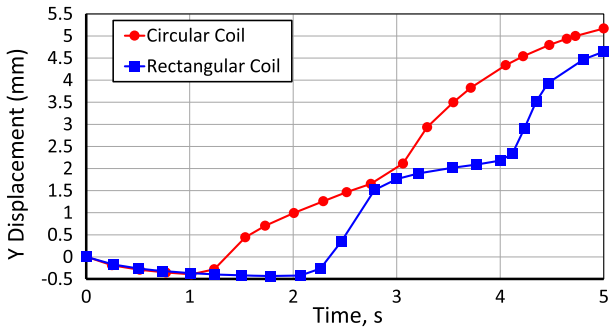

Figure 19. Vertical (*Y*-direction) tip displacement of the SMA beam with circular and rectangular coils. The beam is heated for 5 s using an RMS current of 40 A at 55 kHz. Displacement is referenced from as-loaded (cool) condition. A constant force of 75 N is applied orthogonal to the beam axis and in the direction of the beam short dimension.

system, and electrical power source are designed in an integrated manner. For the torque tube considered in the follow-on effort, an objective such as actuation torque, twist rate, cyclic efficiency, or some combination will be chosen, and the system will be designed to maximize one or more of these objectives subject to constraints. Coil variables are expected to include the diameter of the wires, the shape of the coil, the number of layers, the input current, and driving frequency. The flux concentrator variables are expected to include the shape, material properties, and the location relative to the coil and SMA. Possible cooling methods might include forced convection on the inner and outer surfaces of the tube with cooling fins. Furthermore, the electrical induction system circuit properties should be considered to optimize the power source including the amplifier. In addition to these FEA based analysis objectives and electrical system design, a reduced order model of a thin walled tube being inductively heated will be created to reduce the computation expense of each analysis. This reduced order model will also include the effects of latent heat due to phase transformation and a temperature and phase dependent resistivity.

Acknowledgments

The authors acknowledge Randy Mallari and Mike Gamble of Boeing Research & Technology, who provided experimental data as well as feedback throughout this work. Finite element analysis was performed using an Abaqus research license granted by Simulia.

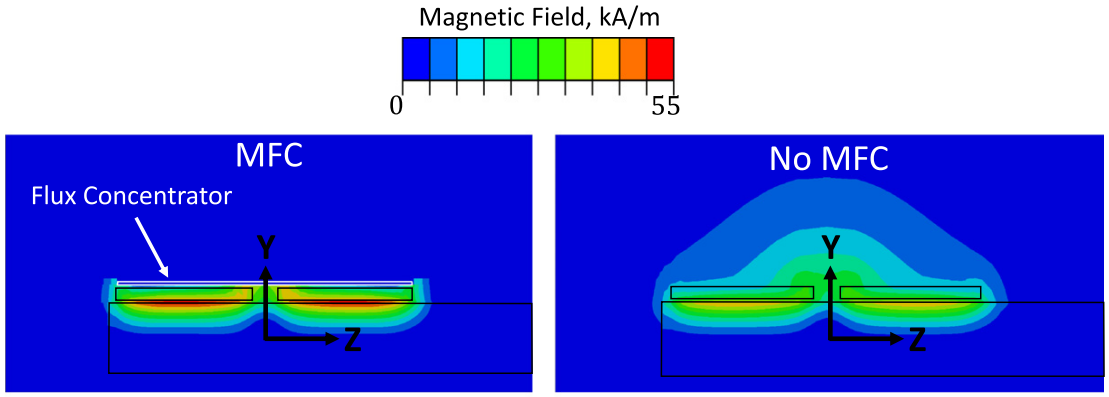

(a) Magnetic field magnitude

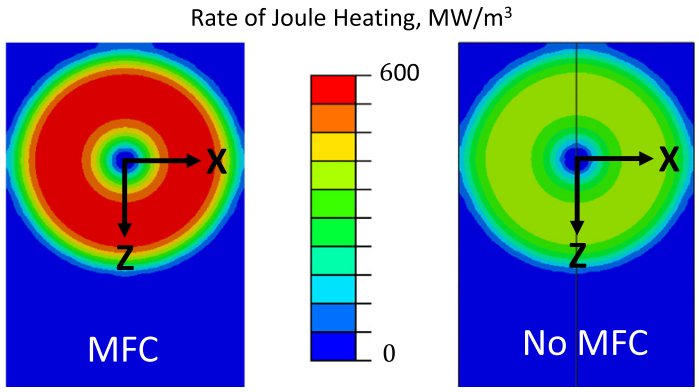

(b) Rate of Joule heating

Figure 20. Electromagnetic fields with and without a NiZn flux concentrator above the coil. The coil is a homogenized 12 turn 20 AWG circular coil with an applied RMS current of 40 A at 55 kHz.

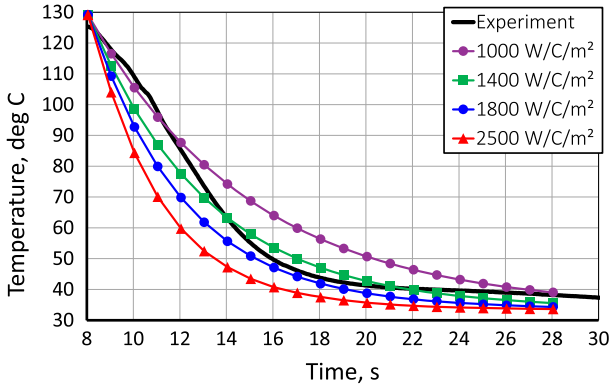

Figure A1. Sample of the parametric study results to determine the effective convection coefficient in the high rate actuation study.

Appendix. Convection cooling study

To calculate a convection coefficient, we must first determine if the flow in the tube is laminar or turbulent and the degree to which is it developed (i.e. hydrodynamically developed, thermally developed, or fully developed). In order for flow to become fully developed, the fluid must travel up to 80 times the inlet diameter, which in our tube is not possible. The vast majority of analytical solutions for tube and pipe flow rely on the assumption that the flow is developed so it is likely that any solution we find for the convection coefficient may not be accurate. Based on the flow speed and fluid properties, it was determined that this flow would be turbulent so we choose to calculate an effective convection coefficient based on the Dittus–Boelter equation [80] which assumes the flow has a constant sink temperature, is hydrodynamically developed, and is thermodynamically developed. Furthermore using a lumped-heat-capacity analysis [24] to test the feasibility of the constant temperature assumption shows that the fluid could be heating significantly before it reaches the end of the tube. Therefor use of the Dittus–Boelter equation with its stated assumptions produces the expectedly poor result shown in figure 12, which is not in good agreement with the experiment. The convection coefficient found in this analysis is 6800 W $°C^{-1}$ m^{-2}.

Rather than moving to a fluid dynamics simulation, we perform a parametric study to determine a convection coefficient that could describe the cooling process. The study assumes the flow enter the tube at the sink temperature and leaves the tube 10 °C above the sink temperature. This change

in temperature over the length of the tube is consist with the result of the previous lumped-heat-capacity analysis. It is assumed that the temperature varies linearly along the length of the tube from the sink temperature to the exit temperature. The parametric study varied the convection coefficient from 500 to 2500 W $°C^{-1}$ m^{-2} in increments of 200. A sampling of this study is shown in figure A1.

The study shows that the convection coefficient should be approximately 1400 W $°C^{-1}$ m^{-2}, which is significantly lower than the calculated value of 6800 W $°C^{-1}$ m^{-2} shown in figure 12. The convection coefficient found from the parametric study is close to what the authors have observed from the literature [80] for similar conditions. While the calculated value is high compared to the parametric study value it is still within a range of values that this fluid mixture could produce. A parametric study is not the ideal method to calculate the cooling coefficients, but it does provide useful data for studies that use this particular high rate actuation setup for future experiments.

References

[1] Lagoudas D C 2008 *Shape Memory Alloys: Modeling and Engineering Applications* (New York: Springer)

[2] Otsuka K and Wayman C M 1999 *Shape Memory Materials* (Cambridge: Cambridge University Press)

[3] Boyd J G and Lagoudas D C 1996 A thermodynamical constitutive model for shape memory materials: I. The monolithic shape memory alloy *Int. J. Plast.* **12** 805–42

[4] Hartl D J and Lagoudas D C 2007 Aerospace applications of shape memory alloys *Proc. Inst. Mech. Eng.* G **221** 535–52

[5] Sanders B, Crowe R and Garcia E 2004 Defense advanced research projects agency-smart materials and structures demonstration program overview *J. Intell. Mater. Syst. Struct.* **15** 227–33

[6] Saunders R N, Herrington J, Hodge L, Hartl D J and Mabe J H 2014 Optimization of a composite morphing wing with shape memory alloy torsional actuators *ASME Smart Materials Adaptive Structures and Intelligent Systems* (American Society of Mechanical Engineers)

[7] Herrington J, Hodge L, Stein C, Babbar Y, Saunders R N, Hartl D J and Mabe J H 2015 Development of a twisting wing powered by a shape memory alloy actuator *AIAA SciTech* (American Institute of Aeronautics and Astronautics Inc.)

[8] Prahlad H and Chopra I 2001 Design of a variable twist tilt-rotor blade using shape memory alloy (SMA) actuators *SPIE's 8th Annual Int. Symp. on Smart Structures and Materials* (International Society for Optics and Photonics) pp 46–59

[9] Kennedy D K, Straub F K, McD Schetky L, Chaudhry Z and Roznoy R 2004 Development of an SMA actuator for in-flight rotor blade tracking *J. Intell. Mater. Syst. Struct.* **15** 235–48

[10] Bertagne C L, Hartl D J and Cognata T J Analysis of highly coupled thermal-structural responses in morphing radiative bodies

[11] Cognata T J, Hartl D J, Sheth R and Dinsmore C 2014 A morphing radiator for high-turndown thermal control of crewed space exploration vehicles

[12] Mabe J H, Ruggeri R T, Rosenzweig E and Chin-Jye M Y 2004 Nitinol performance characterization and rotary actuator design *Smart Structures and Materials* (International Society for Optics and Photonics) pp 95–109

[13] Keefe A C and Carman G P 2000 Thermo-mechanical characterization of shape memory alloy torque tube actuators *Smart Mater. Struct.* **9** 665

[14] Mabe J H, Fischer B and Hartl D J Characterization and modeling of trained nitinol torsional actuators under reverse bias loads *TMS2013 Supplemental Proc.* pp 987–98

[15] Mirzaeifar R, DesRoches R and Yavari A 2010 Exact solutions for pure torsion of shape memory alloy circular bars *Mech. Mater.* **42** 797–806

[16] Hartl D J, Lagoudas D C, Calkins F T and Mabe J H 2010 Use of a ni60ti shape memory alloy for active jet engine chevron application: I. Thermomechanical characterization *Smart Mater. Struct.* **19** 015020

[17] Hartl D J, Mooney J T, Lagoudas D C, Calkins F T and Mabe J H 2010 Use of a Ni60Ti shape memory alloy for active jet engine chevron application: II. Experimentally validated numerical analysis *Smart Mater. Struct.* **19** 015021

[18] Carpenter B and Lyons J 2001 *Eo-1 technology validation report: lightweight flexible solar array experiment* NASA/GSFCLast updated 8 August

[19] Roh J, Han J and Lee I 2005 Finite element analysis of adaptive inflatable structures with SMA strip actuator *Smart Structures and Materials* (International Society for Optics and Photonics) pp 460–71

[20] Collet M, Foltête E and Lexcellent C 2001 Analysis of the behavior of a shape memory alloy beam under dynamical loading *Eur. J. Mech.* A **20** 615–30

[21] Sreekumar M, Singaperumal M, Nagarajan T, Zoppi M and Molfino R 2007 Recent advances in nonlinear control technologies for shape memory alloy actuators *J. Zhejiang Univ. SCI.* A **8** 818–29

[22] Humbeeck J Van 1999 Non-medical applications of shape memory alloys *Mater. Sci. Eng.* A **273** 134–48

[23] Qiu J, Tani J, Osanai D, Urushiyama Y and Lewinnek D 2000 High-speed response of SMA actuators *Int. J. Appl. Electromagn. Mech.* **12** 87–100

[24] Holman J P 1986 Heat transfer

[25] Brinson L C, Bekker A and Hwang S 1996 Deformation of shape memory alloys due to thermo-induced transformation *J. Intell. Mater. Syst. Struct.* **7** 97–107

[26] Huang S, Leary M, Ataalla T, Probst K and Subic A 2012 Optimisation of Ni-Ti shape memory alloy response time by transient heat transfer analysis *Mater. Des.* **35** 655–63

[27] Turner T L, Lach C L and Cano R J 2001 Fabrication and characterization of sma hybrid composites *SPIE's 8th Annual Int. Sym. on Smart Structures and Materials* (International Society for Optics and Photonics) pp 343–54

[28] Pathak A, Brei D and Luntz J 2008 Experimental characterization of the convective heat transfer from shape memory alloy wire to various ambient environments *Student's papers, Pathak A* Mechanical Engineering, University of Michigan2250:481092126

[29] Watkins R T, Shaw J A and Grummon D S 2013 Shape memory thermal lag and superelastic rate sensitivity of SMA cellular structures *SPIE Smart Structures and Materials +Nondestructive Evaluation and Health Monitoring* (International Society for Optics and Photonics) P 86890R

[30] Ertel J D and Mascaro S A 2010 Dynamic thermomechanical modeling of a wet shape memory alloy actuator *J. Dyn. Syst. Meas. Control* **132** 051006

[31] Sun B, Zhang J, Wu X and Liao W 2012 Single-joint driving system of bionic finger based on shape memory alloy *2012 Int. Symp. on Micro-Nano Mechatronicics and Human Sciense (MHS)* (Piscataway, NJ: IEEE)pp 225–8

[32] Hull P V, Canfield S L and Carrington C 2004 A radiant energy-powered shape memory alloy actuator *Mechatronics* **14** 757–75

[33] Maeda S, Abe K, Yamamoto K, Tohyama O and Ito H 1996 Active endoscope with SMA (shape memory alloy) coil springs, In Micro Electro Mechanical Systems *Proc. 9th Int. Workshop on Micro Electromechanical Systems 1996 MEMS'96 An Investigation of Micro Structures, Sensors, Actuators, Machines and Systems* (Piscataway, NJ: IEEE) pp 290–5

[34] Bayer B C, Sanjabi S, Baehtz C, Wirth C T, Esconjauregui S, Weatherup R S, Barber Z H, Hofmann S and Robertson J 2011 Carbon nanotube forest growth on NiTi shape memory alloy thin films for thermal actuation *Thin Solid Films* **519** 6126–9

[35] Webster J 2005 Shape memory material actuation *US Patent App* 11/168545

[36] Davies J and Simpson P 1979 *Induction Heating Handbook* (London: McGraw-Hill)

[37] Mohr R, Kratz K, Weigel T, Lucka-Gabor M, Moneke M and Lendlein A 2006 Initiation of shape-memory effect by inductive heating of magnetic nanoparticles in thermoplastic polymers *Proc. Natl Acad. Sci. USA* **103** 3540–5

[38] Buckley P R, McKinley G H, Wilson T S, Small W, Benett W J, Bearinger J P, McElfresh M W and Maitland D J 2006 Inductively heated shape memory polymer for the magnetic actuation of medical devices *IEEE Trans. Biomed. Eng.* **53** 2075–83

[39] Kabiri Y, Kermanpur A and Foroozmehr A 2012 Comparative study on microstructure and homogeneity of niti shape memory alloy produced by copper boat induction melting and conventional vacuum arc melting *Vacuum* **86** 1073–7

[40] Butler J, Tiernan P, Gandhi A A, Beloshapkin S and Tofail S A M 2011 Processing of small scale nitinol billets by induction heated nonconventional isothermal extrusion (ihncie) *J. Eng. Mater. Technol.* **133** 021009

[41] Frenzel J, Zhang Z, Neuking K and Eggeler G 2004 High quality vacuum induction melting of small quantities of NiTi shape memory alloys in graphite crucibles *J. Alloys Compd.* **385** 214–23

[42] Sanders J O, Sanders A E, More R and Ashman R B 1993 A preliminary investigation of shape memory alloys in the surgical correction of scoliosis *Spine* **18** 1640–6

[43] Giroux E A, Maglione M, Gueldry A and Mantoux J L 1996 Electromagnetic heating of a shape memory alloy translator *J. Phys. D: Appl. Phys.* **29** 923

[44] Tanaka M, Wang F, Abe K, Arai Y, Nakagawa H and Chonan S 2006 A closed-loop transcutaneous power transmission system with thermal control for artificial urethral valve driven by SMA actuator *J. Intell. Mater. Syst. Struct.* **17** 779–86

[45] Chen J C and Wiscombe B 2000 Use of shape memory alloy for internally fixing light emitting device at treatment site *US Patent* 6080160

[46] Hamilton R F, Sehitoglu H, Chumlyakov Y and Maier H J 2004 Stress dependence of the hysteresis in single crystal niti alloys *Acta Mater.* **52** 3383–402

[47] Wetzel E D 2004 Article and method for controlled debonding of elements using shape memory alloy actuators *US Patent* 6773535

[48] Birch N T and Webster J R 2004 Gas turbine engine exhaust nozzle having a noise attenuation device driven by shape memory material actuators *US Patent* 6813877

[49] Takagi T, Luo Y, Suzuki S, Matsumoto M and Tani J 2001 Modeling and numerical simulation onthermomechanical behavior of SMA plates with two-way shape memory effect *J. Intell. Mater. Syst. Struct.* **12** 721–8

[50] Bower A F 2011 *Applied Mechanics of Solids* (Boca Raton, FL: CRC Press)

[51] Tiersten H F 1990 Energy and momentum in the electromagnetic field *A Development of the Equations of Electromagnetism in Material Continua* (Berlin: Springer) pp 105–12

[52] Rudnev V, Loveless D, Cook R L and Black M 2002 *Handbook of Induction Heating* (Boca Raton, FL: CRC Press)

[53] Sadiku M 2014 *Elements of Electromagnetics* (USA: Oxford University Press)

[54] Westgard J B 1996 *Electrodynamics a Concise Introduction* (Berlin: Springer)

[55] Coleman B D and Noll W 1963 The thermodynamics of elastic materials with heat conduction and viscosity *Arch. Ration. Mech. Anal.* **13** 167–78

[56] Coleman B D and Noll W 1964 Material symmetry and thermostatic inequalities in finite elastic deformations *Arch. Ration. Mech. Anal.* **15** 87–111

[57] Lagoudas D C, Hartl D J, Chemisky Y, Machado L and Popov P 2012 Constitutive model for the numerical analysis of phase transformation in polycrystalline shape memory alloys *Int. J. Plast.* **32** 155–83

[58] Patoor E, Lagoudas D C, Entchev P B, Brinson L C and Gao X 2006 Shape memory alloys: I. General properties and modeling of single crystals *Mech. Mater.* **38** 391–429

[59] Lagoudas D C, Entchev P B, Popov P, Patoor E, Brinson L C and Gao X 2006 Shape memory alloys, part ii: Modeling of polycrystals *Mech. Mater.* **38** 430–62

[60] Hartl D J, Lagoudas D C and Calkins F T 2011 Advanced methods for the analysis, design, and optimization of SMA-based aerostructures *Smart Mater. Struct.* **20** 094006

[61] Hartl D J and Lagoudas D C 2009 Constitutive modeling and structural analysis considering simultaneous phase transformation and plastic yield in shape memory alloys *Smart Mater. Struct.* **18** 104017

[62] Hartl D J, Solomou A, Lagoudas D C and Saravanos D 2012 Phenomenological modeling of induced transformation anisotropy in shape memory alloy actuators *SPIE Smart Structures and Materials + Nondestructive Evaluation and Health Monitoring* (International Society for Optics and Photonics) p 83421M

[63] Hartl D J, Kiefer B and Menzel A 2013 Modeling shape memory alloy single crystalline responses using an anisotropic yield surface *TMS2013 Supplemental Proc.* pp 975–86

[64] Mirzaeifar R, DesRoches R, Yavari A and Gall K 2012 Coupled thermo–mechanical analysis of shape memory alloy circular bars in pure torsion *Int. J. Non-Linear Mech.* **47** 118–28

[65] Tabesh M, Lester B T, Hartl D J and Lagoudas D C 2012 Influence of the latent heat of transformation and thermomechanical coupling on the performance of shape memory alloy actuators *ASME 2012 Conf. on Smart Materials, Adaptive Structures and Intelligent Systems* (American Society of Mechanical Engineers) pp 237–48

[66] Oehler S D, Hartl D J and Lagoudas D C 2011 Analysis and optimization of improved hybrid SMA flexures for high rate actuation *SPIE Smart Structures and Materials+ Nondestructive Evaluation and Health Monitoring* (International Society for Optics and Photonics) p 797907

[67] Fisk M 2008 Simulation of Induction Heating in Manufacturing *PhD thesis* Division of Material Mechanics Luleå University of Technology

[68] 2013 Abaqus *Abaqus 6.13 Online Documentation* Dassault Systemes of America Corp.

[69] Qidwai M A and Lagoudas D C 2000 Numerical implementation of a shape memory alloy thermomechanical constitutive model using return mapping algorithms *Int. J. Numer. Methods Eng.* **47** 1123–68

[70] Lagoudas D, Bo Z, Qidwai M and Entchev P 2003 *SMA um: User material subroutine for thermomechanical constitutive*

model of shape memory alloys Texas A&M University College Station TX

[71] Bay F, Labbé V, Favennec Y and Chenot J L 2003 A numerical model for induction heating processes coupling electromagnetism and thermomechanics *Int. J. Numer. Methods Eng.* **58** 839–67

[72] Buehler W J and Wang F E 1968 A summary of recent research on the nitinol alloys and their potential application in ocean engineering *Ocean Eng.* **1** 105–20

[73] Hediehloo M and Akhbari M 2009 New approach in design of planar coil of induction cooker based on skin and proximity effects analysis *2009 IEEE Int. Conf. on Industrial Technology (ICIT'09)* (Piscataway, NJ: IEEE) pp 1–6

[74] Zhu T, Feng P, Li X, Li F and Rong Y 2013 The study of the effect of magnetic flux concentrator to the induction heating system using coupled electromagnetic-thermal simulation model *Int. Conf. on Mechanical and Automation Engineering (MAEE 2013)* (Piscataway, NJ: IEEE) pp 123–7

[75] Ruffini R T, Nemkov V and Vyshinskaya N 2004 New magnetodielectric materials for magnetic flux control *Proc. Int. Symp. HES-04 Heating by Electromagnetic Sources (Padua, Italy)*

[76] Ruffini R S, Ruffini R T and Nemkov V S 1998 Advanced design of induction heat treating coils: II. Magnetic flux concentration and control *Ind. Heat.* **65** 69–72

[77] Morrison S A, Cahill C L, Carpenter E E, Calvin S, Swaminathan R, McHenry M E and Harris V G 2004 Magnetic and structural properties of nickel zinc ferrite nanoparticles synthesized at room temperature *J. Appl. Phys.* **95** 6392–5

[78] Srinivasan T T, Ravindranathan P, Cross L E, Roy R, Newnham R E, Sankar S G and Patil K C 1988 Studies on high-density nickel zinc ferrite and its magnetic properties using novel hydrazine precursors *J. Appl. Phys.* **63** 3789–91

[79] Nian S C, Huang M S and Tsai T H 2014 Enhancement of induction heating efficiency on injection mold surface using a novel magnetic shielding method *Int. Commun. Heat Mass Transfer* **50** 52–60

[80] Janna W S 1999 *Engineering Heat Transfer* (Boca Raton, FL: CRC Press)